ATLAS NOTE

ATLAS-CONF-2016-072

4th August 2016

Search for single production of vector-like quarks decaying into Wb in pp collisions at $\sqrt{s} = 13$ TeV with the ATLAS detector

The ATLAS Collaboration

Abstract

A search for singly-produced vector-like quarks Q, where Q can be either a T quark with charge 2/3 or a Y quark with charge 4/3, is performed in 3.2 fb^{-1} of proton–proton collision data at a centre-of-mass energy of 13 TeV recorded with the ATLAS detector at the LHC. The analysis targets $Q \to Wb$ decays where the W boson decays leptonically. No significant excess over Standard Model backgrounds is observed and upper limits on the $Q \to Wb$ cross-section times branching ratio are set as a function of the vector-like quark mass. For a QWb coupling strength of $\sqrt{(c_{\mathrm{L}}^{Wb})^2 + (c_{\mathrm{R}}^{Wb})^2} = 1/\sqrt{2}$, the observed (expected) 95% confidence level lower limit on the Y-quark mass is 1.44 TeV (1.45 TeV). The results are also interpreted as limits on the QWb coupling strength and the mixing with the Standard Model sector for a singlet T quark or a Y quark from a (B, Y) doublet. The smallest excluded coupling-strength values are obtained for vector-like quark masses around 1000 GeV; they are as small as $|c_L^{Wb}| = 0.45$ for a T quark and $\sqrt{(c_{\mathrm{L}}^{Wb})^2 + (c_{\mathrm{R}}^{Wb})^2} = 0.33$ for a Y quark. Within a (B, Y) doublet model, the excluded mixing parameter, $|\sin\theta_R|$, in this mass region is comparable to the exclusion limits from electroweak precision observables.

ATLAS-CONF-2016-072
08 August 2016

1 Introduction

While it is generally accepted that the Standard Model (SM) has three fermion generations, the number of generations is not fixed by the theory and there are many models that predict the existence of additional quarks [1, 2]. The nature of these heavy quarks can be SM-like (chiral) or vector-like. The discovery of a SM-like Higgs boson at the LHC [3, 4] excludes a perturbative, fourth generation of chiral quarks [5], since their contribution to loop-mediated Higgs boson couplings would have altered the cross section and the decay rates of the Higgs boson. However, this does not rule out vector-like quarks (VLQ). Vector-like quarks are hypothetical spin-1/2 colored particles with left-handed and right-handed components that transform in the same way under the SM gauge group and therefore their masses are not generated by a Yukawa coupling to the Higgs boson [6]. The effects on Higgs production and decay rates of loop diagrams including VLQs are well below the precision of the current measurements [6]. In many models, VLQs mix with the SM quarks predominantly of the third generation due to the large masses of the bottom and top quark [7, 8]. They are also able to stabilize the electroweak vacuum [9]. VLQs appear in several extensions of the SM that address the hierarchy problem, such as extra dimensions [10], composite Higgs [11, 12] and Little Higgs [13] models, where they are added to the SM in multiplets. They can also appear in supersymmetric models [14].

This analysis concentrates on searches for single production of heavy vector-like Q quarks produced via Wb fusion, $pp \rightarrow Qqb + X$, with a subsequent $Q \rightarrow Wb$ decay. Here Q can be either a T quark with charge $+2/3$ or a Y quark with charge $-4/3$ or their anti-quarks. An example of a leading-order (LO) Feynman diagram is presented in Figure 1.

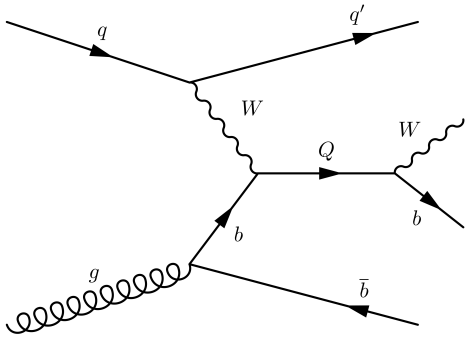

Figure 1: Leading-order Feynman diagram of single Q ($Q = T, Y$) production in Wb fusion and subsequent decay into Wb.

Vector-like T quarks can belong to any multiplet, while Y quarks cannot exist as singlets. The interpretation used in this analysis focuses on Y quarks from a (B, Y) doublet and on singlet T quarks. For such T quarks, the branching ratios (BRs) are model and mass dependent, but in the high-mass limit converge towards 2:1:1 (Wb:Zt:Ht). Due to its charge, the Y quark can decay only to Wb and therefore $BR(Y \rightarrow Wb) = 100\%$. The single production of vector-like quarks is enabled by their coupling to SM quarks. As a result, searches for singly-produced VLQs can be used to probe these couplings. At high VLQ masses, single VLQ production can become the dominant production mechanism at the LHC, depending on the strength of this coupling. The results are presented here for two different models that use a different formulation of the Lagrangian embedding these new particles and their interactions, namely that

in Ref. [6], where a mixing term between the SM and vector-like quarks is introduced in a renormalisable extension of the SM, and in Refs. [15, 16], which use a phenomenological Lagrangian parameterised with coupling terms, but is non-renormalisable. The two main differences of these approaches are additional terms present in Refs. [15, 16], that allow for larger production cross-sections, and the complete description of the multiplet-dimension dependence of the BR in Ref. [6]. The model interpretation in terms mixing angles θ (θ_L, θ_R) within a given multiplet described in Ref. [6] connects the left- and right-handed mixing angles and fully determines all BRs for any given heavy quark mass. For the interpretation in terms of coupling terms c_{L}^{Wb} and c_{R}^{Wb} as introduced in Refs. [15, 16], assumptions must be made about the $Q \to Wb, Q \to Zt$ and $Q \to Ht$ BRs. A comparison of the respective Lagrangians of both models yields a simple relation between $\sin\theta_{R,L}$ and $c_{\mathrm{R,L}}^{Wb}$: $c_{\mathrm{R,L}}^{Wb} = \sqrt{2}\sin\theta_{R,L}$. The relative contribution of the left- and right-handed components of the mixing and coupling also depends on the dimension of the VLQ multiplet. For T singlets, the left-handed components ($\sin\theta_{\mathrm{L}}$ and c_{L}^{Wb}) are dominant. When no multiplet model is specified, the results for Y quarks are presented in terms of the magnitude of the total coupling $\sqrt{(c_{\mathrm{L}}^{Wb})^2 + (c_{\mathrm{R}}^{Wb})^2}$. For a (B, Y) doublet model, results are interpreted in terms of the dominant right-handed ($\sin\theta_{\mathrm{R}}$) component [6]. The formulation of Ref. [6] also allows comparisons of constraints on mixing angles within a certain multiplet model from electroweak precision observables, such as the ratio R_b of the partial width for $Z \to b\bar{b}$ to the total hadronic Z-boson width and the oblique parameters S and T [17], which can be compared with the constraints obtained from a direct search.
The ATLAS and CMS collaborations have published searches for single and pair-production of vector-like T quarks in all three decay channels [18–27]. Assuming a BR of 100% for the corresponding decay channel, the best observed limits on the pair-produced T-quark mass are $m_T > 900$ GeV for $T \to Ht$ [25], 810 GeV for $T \to Zt$ [19] and 920 GeV for $T \to Wb$ [22] decay channels at the 95% confidence level (CL), independent from the size of the c^{Wb} coupling strengths. These searches also report limits as a function of the assumed BRs into the three decay modes. The best observed 95% CL limits are $m_T > 800$ GeV and $m_T > 750$ GeV for a weak-isospin doublet and singlet, respectively [18]. For single T-quark production, searches for T quarks with decays into Zt [19] and Wb [24] have been carried out by the ATLAS Collaboration using the Run 1 dataset at $\sqrt{s} = 8$ TeV. T quarks in the $T \to Zt$ decay channel with masses between 450 GeV to 650 GeV assuming a mixing parameter as low as 0.7 are excluded at 95% CL [19], while T quarks in the $T \to Wb$ decay channel with masses below 950 GeV are excluded at 95% CL, assuming a unit coupling and BR($T \to Wb$) = 0.5. The CMS collaboration has published new results studying single T quark production using the Run 2 dataset at $\sqrt{s} = 13$ TeV collected in 2015 [27–29] that set upper limits at 95% CL on single T quark production cross-section times BR($T \to tH$) that varies between 0.31 pb and 0.93 pb for T quark masses in the range 1000-1800 GeV [28], as well as on single T quark production cross-section times BR($T \to Zb$) that varies between 0.97 and 0.16 pb (0.6-0.14 pb) for T quark masses in the range 700-1700 GeV in the right (left) handed Tb (Tt) production channel [27]. For a mass of 1000 GeV, a production cross-section times branching fraction above 0.9 pb (0.6 pb) is excluded at 95% CL for the $T \to Ht$ decay channel assuming left-handed (right-handed) coupling of the T quark to SM particles [29].

This note describes a search for $Q \to Wb$ ($Q = T$ or Y) production, with the prompt W-boson decaying leptonically, giving a lepton + jets signature characterised by the presence of exactly one electron or muon, two or more jets and missing transverse momentum from the escaping neutrino. It is assumed that Y and T quarks are produced in Wb fusion only. For a T singlet, Zt fusion could contribute as well. However, since the corresponding cross-section is expected to be much smaller, this contribution is neglected. Since the kinematic distributions of the decay products for the T quark and Y quark in the Wb decay channel are the same, only Y signal samples are generated and used to derive the results for

the Tqb signals. Other possible decay modes of the T quark ($T \to Zt$, $T \to Ht$) are assumed to have negligible acceptance in this search. Due to the tight selection cuts, contributions from $Tt(q)$ associated production are also considered to be negligible. The analysis is optimized to search for massive VLQs with a high-momentum single b-jet in the final state. The b-jet and the charged lepton originating from the Q decay are approximately back-to-back in the transverse plane since both originate from the decay of a heavy object. The outgoing light quark in the process depicted in Figure 1 often produces a jet in the forward region of the detector. The second b-jet from the gluon splitting may be observed in either the forward or central region. Since this b-jet is typically soft, it often falls outside the detector acceptance.

The main background processes with a single-lepton signature arise from top-quark pair production, single top-quark production and W-boson production in association with jets (W+jets), with smaller contributions from Z-boson production in association with jets (Z+jets) and from diboson (WW, WZ, ZZ) production. Multijet events also contribute to the selected sample via the misidentification of a jet or a photon as an electron or the presence of a non-prompt electron or muon. To estimate these SM backgrounds in a consistent and robust fashion, two control regions (CRs) are defined. They are chosen to be non-overlapping with the signal region (SR) selection in order to provide independent data samples enriched in particular background sources. The shape of the discriminating variable, the invariant mass of the heavy quark candidate, is used in a binned likelihood fit to test for the presence of a signal. The systematic uncertainties and the statistical uncertainties on the signal and background expectations are included in the fit via nuisance parameters. Correlations of a given nuisance parameter across the various regions, between the various backgrounds, and possibly the signal, are also taken into account. A background-only fit to the SR and CRs is used to determine the compatibility of the observed event yield in the SR with the corresponding SM background expectation. Using templates from the SR and CRs, binned profile likelihood fits are performed to estimate the Y/T VLQ production cross-sections.

The note is organised as follows: Section 2 describes briefly the ATLAS detector. Section 3 presents the reconstruction of objects in ATLAS and the event selection. The samples of simulated events used for the analysis are summarised in Section 4. Section 5 describes the analysis strategy, and systematic uncertainties are discussed in Section 6. Exclusion limits in terms of cross section times branching ratios are presented in Section 7, together with their interpretation as coupling and mixing angle limits. Finally, a summary is given in Section 8.

2 ATLAS detector

The ATLAS detector [30] at the LHC is a multi-purpose particle detector with a forward-backward symmetric cylindrical geometry and covers nearly the entire solid angle around the collision point.[1] It consists of an inner tracking detector (ID) surrounded by a thin superconducting solenoid magnet producing an axial 2 T magnetic field, a fine-granularity electromagnetic (EM) and hadronic calorimeters, and a muon spectrometer (MS) incorporating three large air-core toroid magnet assemblies. The ID consists of a high-granularity silicon pixel detector, including the newly-installed insertable B-layer (IBL) [31], and a silicon microstrip tracker, together providing charged particle tracking information in the pseudorapidity

[1] ATLAS uses a right-handed coordinate system with its origin at the nominal interaction point (IP) in the centre of the detector. The positive x-axis is defined by the direction from the IP to the centre of the LHC ring, with the positive y-axis pointing upwards, while the beam direction defines the z-axis. Cylindrical coordinates (r, ϕ) are used in the transverse plane, ϕ being the azimuthal angle around the z-axis. The pseudorapidity η is defined in terms of the polar angle θ by $\eta = -\ln\tan(\theta/2)$.

region $|\eta| < 2.5$. It is surrounded by a transition radiation tracker, which enhances electron identification information in the region $|\eta| < 2.0$. The EM calorimeter is a lead-liquid argon sampling detector, divided into a barrel region ($|\eta| < 1.475$) and two end-cap ($1.375 < |\eta| < 3.2$) regions, and provides energy measurements of electromagnetic showers. Hadron calorimetry is also based on the sampling technique, with either scintillator tiles or liquid argon as the active medium and with steel, copper, or tungsten as the absorber material. The calorimeters cover in total a region of $|\eta| < 4.9$. The MS measures the deflection of muons with $|\eta| < 2.7$ using three layers of high-precision tracking chambers located in a toroidal field of approximately 0.5 T and 1 T in the central and end-cap regions of ATLAS, respectively. The MS is also instrumented with separate trigger chambers covering $|\eta| < 2.4$. A two-level trigger system [32], using custom hardware followed by a software-based level, is used to reduce the trigger rate to a maximum of around 1 kHz for offline storage.

3 Object reconstruction and event selection

The data used in this search correspond to an integrated luminosity of 3.2 ± 0.1 fb^{-1} of pp collisions with 25 ns bunch spacing recorded between August and November 2015 with the ATLAS detector at a centre-of-mass energy of $\sqrt{s} = 13$ TeV. The luminosity uncertainty is derived following the same methodology as detailed in Ref. [33]. The average number of interactions per pp bunch crossing ranged from approximately 5 to 25, with a mean of 14. Only runs with stable beam collisions and all relevant ATLAS detector components fully functional are used.

The final states considered in this search require the presence of one charged lepton candidate (electron or muon) and multiple hadronic jets. Events are required to pass single-electron or single-muon triggers with transverse momentum (p_{T}) thresholds at 24 GeV in the case of electrons and 20 GeV in the case of muons. These triggers with a low p_{T} threshold and, in case of muon triggers, with lepton isolation requirements, are combined in a logical OR with higher-threshold triggers without isolation to give maximum efficiency. In addition, events must have at least one reconstructed vertex with two or more tracks above 0.4 GeV that is consistent with the beam-collision region in the $x - y$ plane. If multiple vertices are reconstructed, the vertex with the largest sum of the squared p_{T} of its associated tracks is taken as the primary vertex. For the final states considered in this analysis, the vertex reconstruction and selection efficiency is close to 100%.

Electrons candidates [34–36] are reconstructed from isolated energy deposits (clusters) in the EM calorimeter, each associated to a reconstructed ID track within the fiducial region of $|\eta_{\mathrm{cluster}}| < 2.47$, where η_{cluster} is the pseudorapidity of the calorimeter energy deposit associated with the electron candidate. An additional veto is placed on electrons in the calorimeter transition region between the barrel and end-cap electromagnetic calorimeters, $1.37 < |\eta_{\mathrm{cluster}}| < 1.52$. Electrons must pass the tight likelihood identification criterion described in Ref. [36], based on shower-shape and track-matching variables, and need to have a transverse energy $E_{\mathrm{T}} = E_{\mathrm{cluster}}/\cosh(\eta_{\mathrm{track}}) > 25$ GeV, where E_{cluster} indicates the electromagnetic cluster energy and η_{track} the track pseudorapidity [34]. Muons are reconstructed [37, 38] by combining matching tracks reconstructed in both the ID and the MS, using the complete track information of both detectors and accounting for material effects of the ATLAS detector structure. The muon candidates must pass the medium selection criteria [38] and are required to be in the central region of $|\eta| < 2.5$. To reduce the contribution of leptons from hadronic decays (non-prompt leptons), both electrons and muons must satisfy isolation criteria that include both track and calorimeter information tuned for an overall efficiency

of 98%, independent of the p_{T} of the lepton. Electron and muon candidates are required to be isolated from additional tracks within a cone around their directions with a radius of $\Delta R \equiv \sqrt{(\Delta\eta)^2 + (\Delta\phi)^2}$ [39] with $\Delta R = \min(0.2, 10\ \mathrm{GeV}/p_{\mathrm{T}})$ [36] for electrons and $\Delta R = \min(0.3, 10\ \mathrm{GeV}/p_{\mathrm{T}})$ for muons [38]. The electron (muon) calorimeter-based isolation variable is defined as the sum of the calorimeter transverse energy deposits in a cone of size $\Delta R = 0.2$, after subtracting the contribution from the energy deposit of the electron (muon) itself and correcting for pile-up effects, divided by the electron (muon) p_{T}. The final isolation selection criteria are determined using the relative isolation variables, which are defined as the ratio of the track- or calorimeter-based isolation variables to the transverse momentum of the electron or muon, respectively. Finally, the lepton tracks are matched to the primary vertex of the event by requiring the longitudinal impact parameter z_0 to satisfy $|z_0 \sin\theta_{\mathrm{track}}| < 0.5$ mm, where θ_{track} is the polar angle of the track.[2] The significance of the transverse impact parameter d_0, calculated with respect to the measured beam line position, is required to satisfy $|d_0/\sigma(d_0)| < 5$ for electrons and $|d_0/\sigma(d_0)| < 3$ for muons, where $\sigma(d_0)$ is the uncertainty on d_0.

Jets are reconstructed from three-dimensional topological calorimeter energy clusters [40] using the anti-k_T algorithm [41] with a radius parameter 0.4. Each topological cluster is calibrated to electromagnetic scale response prior to jet reconstruction [42, 43]. The reconstructed jets from the clusters are then calibrated to the particle level by the application of a correction derived from simulation and dedicated calibration data samples at $\sqrt{s} = 13$ TeV. Data quality criteria [44, 45] are imposed to identify jets arising from non-collision sources or detector noise, and any event containing at least one such jet is removed [46]. Finally, jets considered in this analysis are required to have $p_{\mathrm{T}} > 25$ GeV. The pseudorapidity acceptance for jets differs between different selections: central jets are required to have $|\eta| < 2.5$, while forward jets are defined to have $2.5 < |\eta| < 4.5$. Furthermore, jets with a $p_T < 60$ GeV and $|\eta| < 2.4$ are required to satisfy criteria, implemented in the jet vertex tagger algorithm [47], designed to select jets that originate from the hard scattering and reduce the effect of in-time pileup. For the selection of events containing a top quark in the decay, the identification of jets emerging from b-quark decays (b-tagging) is beneficial. These jets are tagged using the long lifetime of b hadrons resulting in a significant flight path length. The secondary decay vertex from such hadrons is measurable with respect to the primary vertex. To identify jets containing b-hadrons (henceforth referred to as b-jets) and to suppress $t\bar{t}$ background in the SR, a multi-variate discriminant is used that combines information on the impact parameters of inner detector tracks associated to the jet, the presence of displaced secondary vertices, and the reconstructed flight paths of b- and c-hadrons inside the jet [48–50]. Jets are considered as being b-tagged if the value of the multivariate discriminant is larger than a certain threshold. The criterion in use is only calculated for central jets ($|\eta| < 2.5$) with $p_{\mathrm{T}} > 20$ GeV and has an efficiency of approximately 77% for b-jets in simulated $t\bar{t}$ events. The tagging algorithm gives a rejection factor of 126 against light quark and gluon jets and of 4.5 against jets originating from charm quarks [51].

To avoid counting a single detector response as two objects, an overlap removal procedure is used. Jets overlapping with identified electron candidates within a cone of $\Delta R = 0.2$ are removed from the list of jets, as the jet and the electron are very likely to be the same physics object. If the nearest jet surviving the selection described above is within $\Delta R = 0.4$ of the electron, the electron is discarded, to ensure it is sufficiently separated from nearby jet activity. Muons are removed if they are separated from the nearest jet by $\Delta R < 0.4$, to reduce the background from muons from heavy-flavour decays inside jets. However, if this jet has fewer than three associated tracks, the muon is kept and the jet is removed instead; this

[2] The longitudinal impact parameter z_0 is the difference between the longitudinal position of the track along the beam line at the point where the transverse impact parameter (d_0) is measured and the longitudinal position of the primary vertex.

avoids an inefficiency for high-energy muons undergoing significant energy loss in the calorimeter.

The missing transverse momentum ($E_{\mathrm{T}}^{\mathrm{miss}}$) is a measure of the momentum of the escaping neutrinos. It also includes energy losses due to detector inefficiencies and its resolution, leading to the mis-measurement of the true E_{T} of the final interacting objects. It is defined as the vector momentum imbalance in the transverse plane, obtained from the negative vector sum of the momenta of all particles detected in a proton-proton collision [52, 53]. The $E_{\mathrm{T}}^{\mathrm{miss}}$ reconstruction is based on the selected leptons, photons and jets found in the event. Its value is evaluated by the vector sum of the p_{T} of the physics objects selected in the analysis and the tracks not belonging to any of these physics objects [52]. Jets used in the $E_{\mathrm{T}}^{\mathrm{miss}}$ calculation are reconstructed from clusters of calorimeter cells with $|\eta| < 5$ using the anti-k_T algorithm with a radius parameter of 0.4. They are required to have a $p_{\mathrm{T}} > 20$ GeV.
Events of interest must have exactly one identified lepton (electron or muon) with $p_{\mathrm{T}} > 25$ GeV that must be matched to the lepton selected by the a trigger, and at least one central jet with a $p_{\mathrm{T}} > 25$ GeV satisfying the quality and kinematic criteria discussed above. In case there are any forward jets in the event, it is required that their transverse momentum is larger than 40 GeV. The missing transverse energy $E_{\mathrm{T}}^{\mathrm{miss}}$ is required to be larger than 120 GeV in order to suppress diboson and multijet events. In the following and unless stated otherwise, only events satisfying this selection, referred to as "preselection", are considered.

4 Signal and background modelling

Monte Carlo (MC) simulation samples are used to model the expected signal and SM background distributions. The MC samples are processed either through the full ATLAS detector simulation [54] based on GEANT4 [55] or through a faster simulation making use of parametrised showers in the calorimeters [56]. Effects of both in-time and out-of-time pileup, from additional pp collisions in the same and nearby bunch crossings, are modelled by overlaying minimum-bias interactions generated with PYTHIA 8.186 [57] according to the luminosity profile of the recorded data. The distribution of the number of additional pp interactions in the MC samples is reweighed to match the pileup conditions observed in data. All simulated samples use EVTGEN [58] to model the decays of heavy flavour hadrons, except for processes modelled using the SHERPA generator [59]. All simulated MC events are processed using the same reconstruction algorithms and analysis chain as for the data, but small corrections are applied to trigger and object reconstruction efficiencies, as well as detector resolutions, to better model the observed response.

4.1 Signal modelling

Simulated events for signal processes are generated at leading order (LO) in the four-flavour scheme (4FS) with the MADGRAPH5 [60] generator using the NNPDF2.3 parton distribution function (PDF) set [61], and interfaced to PYTHIA8 [62] for parton showering and hadronisation. Samples of Yqb signals are produced for masses ranging from 700 GeV to 1600 GeV in steps of 100 GeV with equal left-handed and right-handed coupling strengths of size of 0.5 [63] corresponding to $\sqrt{(c_{\mathrm{L}}^{Wb})^2 + (c_{\mathrm{R}}^{Wb})^2} \approx 1/\sqrt{2}$ to a very good

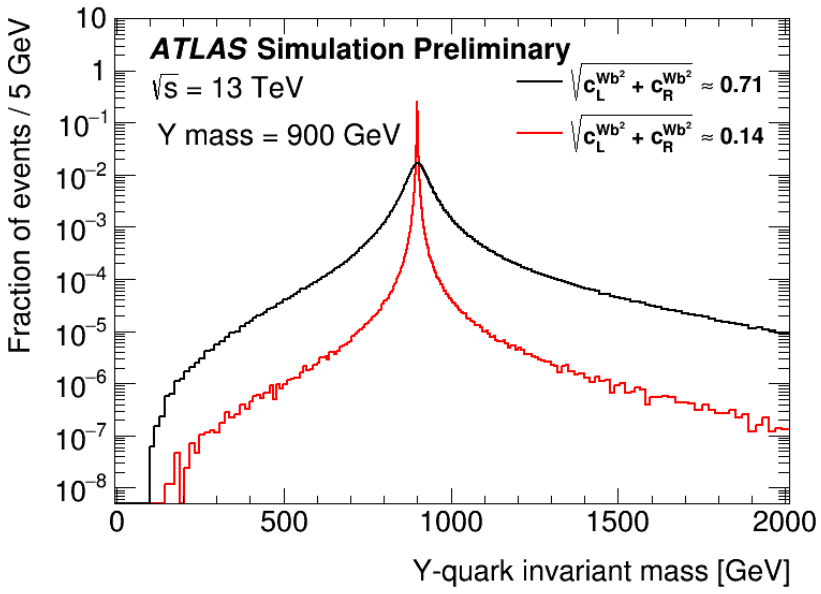

Figure 2: Comparison of truth vector-like Y quark mass distribution with a mass of 900 GeV for a coupling strength of 0.5 ($\sqrt{(c_{\mathrm{L}}^{Wb})^2 + (c_{\mathrm{R}}^{Wb})^2} \approx 0.71$, black line) and of 0.1 ($\sqrt{(c_{\mathrm{L}}^{Wb})^2 + (c_{\mathrm{R}}^{Wb})^2} \approx 0.14$, red line) as defined in Ref. [63].

approximation.[3] The kinematics of the final-state particles are very similar for left-handed and right-handed couplings and hence the acceptance for both chiralities is assumed to be equal. The LO cross-sections calculated for the signal processes in the simulation are normalised to the next-to-leading order (NLO) theory benchmark calculation taken from Ref. [64, 65]. The single-production cross-sections and the decay widths of the VLQ resonances are mass- and coupling-dependent as shown in Figure 2. In order to test the signal acceptance for different signal couplings, a reweighting method is developed. In this reweighting procedure, simulated signal samples produced with the nominal coupling strength of 0.5 are corrected on an event-by-event basis using reweighting factors obtained by comparing the target and the nominal VLQ mass distributions of generated truth signal samples. The method is validated with fully reconstructed signal samples with varied coupling strengths.

4.2 Background modelling

The $t\bar{t}$ events are generated with the NLO generator Powheg-Box 2.0 [66–69] using the CT10 PDF set [70], interfaced to Pythia 6.428 [71] with the CTEQ6L PDF set [72] and the Perugia 2012 (P2012) underlying event (UE) tune [73]. The hard process factorisation scale μ_f and renormalisation scale μ_r are set to the default Powheg-Box value. $\mu = (m_t^2 + p_{\mathrm{T,top}}^2)^{1/2}$, where m_t and $p_{\mathrm{T,top}}$ are the top quark mass $m_t = 172.5$ GeV and transverse momentum evaluated for the underlying Born configuration, respectively. The Powheg-Box model parameter h_{damp}, which controls matrix element to parton shower matching in Powheg-Box and effectively regulates the high-p_{T} radiation, is set to $m_t = 172.5$ GeV, a setting that was found to best describe the $t\bar{t}$ system p_{T} at $\sqrt{s} = 7$ TeV [74]. The sample is generated assuming top quark

[3] The coupling parameter κ_T in [63] used for the signal production is related to the coupling parameters $c_{L/R}^{Wb}$ in [64, 65] via $\kappa_T f(M) = c_{L/R}^{Wb}/\sqrt{2}$, where $f(M) \approx \sqrt{1/(1 + O(M_Q^{-4}))}$ and therefore $\kappa_T \approx c_{L/R}^{Wb}/\sqrt{2}$ to a very good approximation.

decays exclusively through $t \to Wb$.

Alternative $t\bar{t}$ samples are produced to model uncertainties on this process. The effects of initial- and final-state radiation (ISR/FSR) are explored using two alternative Powheg-Box 2.0 +Pythia 6.428 samples, one with h_{damp} set to $2m_t$, the renormalisation and factorisation scales set to half the nominal value and using the P2012 high-variation UE tune, giving more radiation, and another with the P2012 low-variation UE tune, $h_{\text{damp}} = m_t$ and the renormalisation and factorisation scales set to twice the nominal value, giving less radiation [75]. The μ_r and μ_f scale variations and the h_{damp} variations are varied together because these two proposed variations are found to cover the full set of uncertainties obtained by changing the scales and the hdamp parameter independently. To provide a comparison to a different parton shower model, an additional $t\bar{t}$ sample is generated using the same Powheg-Box model setup as for the nominal Powheg-Box 2.0 + Pythia 6.428 sample, while parton shower, hadronisation, and UE are simulated with Herwig++ 2.7.1 [76] with the UEEE5 tune [77] and the corresponding CTEQ6L1 PDF set. Additional $t\bar{t}$ simulation samples are generated using Madgraph5_aMC@NLO 2.2.1 [78] interfaced to Herwig++ 2.7.1 to determine the systematic uncertainties related to the use of different models for the hard scattering generation, while maintaining the same parton shower model.

All $t\bar{t}$ samples are normalised to the theoretical cross-section value for the inclusive $t\bar{t}$ process of 832^{+46}_{-51} pb obtained with Top++ [79], performed at next-to-next-to-leading order (NNLO) in QCD and including resummation of next-to-next-to-leading logarithmic (NNLL) soft gluon terms [80–84]. Theoretical uncertainties result from variations of the factorisation and renormalisation scales, as well as from uncertainties on the PDF and α_S. The latter two represent the largest contribution to the overall theoretical uncertainty on the cross-section and are calculated using the PDF4LHC prescription [85].

Single top-quark background processes corresponding to the Wt and s-channel production mechanisms are generated with Powheg-Box 2.0 [66–69] using the CT10 PDF set. Overlaps between the $t\bar{t}$ and Wt final states are removed using the "diagram removal" scheme [67]. The t-channel single top-quark events are generated using the Powheg-Box 1.0 [86] NLO generator that uses the 4FS. The fixed four-flavour PDF set CT10f4 [70] is used for the matrix-element calculations. All single top-quark samples are normalised to the approximate NNLO theoretical cross-sections [87–89]. To model the parton shower, hadronisation and underlying event Pythia 6.428 with the P2012 tune is used. Additional single top-quark samples are generated using the same Powheg-Box model setup as for the nominal sample, while parton shower, hadronisation, and UE are simulated with Herwig++ 2.7.1 [76]. ISR/FSR effects are explored using alternative Powheg-Box 2.0 + Pythia 6.428 samples with P2012 high- and low-variation UE tune that are compared to the nominal samples. Additional single top quark samples are generated using Madgraph5_aMC@NLO 2.2.1 interfaced to Herwig++ 2.7.1 to determine the systematic uncertainties associated with the choice of the NLO generator.

Samples of W/Z+jets events are generated with the Sherpa 2.2.0 [59] generator. The matrix-element calculation is performed up to two partons at NLO and up to four partons at LO using Comix [90] and OpenLoops [91]. The matrix element calculation is merged with the Sherpa parton shower [92] using the ME+PS@NLO prescription [93]. The PDF set used for the matrix element calculation is CT10 with a dedicated parton shower tuning developed by the Sherpa authors. The W+jets and Z+jets samples normalised to the NNLO theoretical cross-sections for inclusive W and Z production calculated with FEWZ [94].

Diboson events ($WW/WZ/ZZ$+jets) with one of the bosons decaying hadronically and the other leptonically are generated with the NLO generator Sherpa 2.1.1 and include processes containing up to four

electroweak vertices. The matrix-element includes up to 1 (ZZ) or 0 (WW, WZ) additional partons at NLO and up to 3 partons at LO using the same procedure as for W/Z+jets. All diboson samples are normalised to their NLO theoretical cross-sections provided by SHERPA. In table 1 the main parameters of the MC samples used in this search are summarised.

Process	Generator + parton showering/hadronisation	Tune	PDF set	Inclusive cross-section order in pQCD
Y signal sample	MADGRAPH5 + PYTHIA 8.186	A14	NNPDF2.3	NLO
$t\bar{t}$	POWHEG-BOX 2.0 + PYTHIA 6.428	P2012	CT10	NNLO+NNLL
Single top	POWHEG-BOX 2.0 + PYTHIA 6.428	P2012	CT10	NNLO+NNLL
Dibosons WW, WZ, ZZ	SHERPA 2.1.1	Default	CT10	NLO
W/Z + jets	SHERPA 2.2.0	Default	CT10	NNLO

Table 1: List of generators used to model the different background processes. Information is given about the perturbative QCD (pQCD) highest-order accuracy used for the normalisation of the different samples, the underlying event tunes and PDF sets considered. All processes, except for Yqb signals, are generated at NLO in QCD. The LO cross-sections calculated for the Yqb signal processes in the simulation are normalised to the NLO theoretical cross-section taken from Ref. [64, 65]

4.3 Estimation of non-prompt and fake lepton backgrounds

Background processes involving non-prompt leptons, hadrons and photons may satisfy the selection criteria, giving rise to so called "non-prompt and fake" lepton backgrounds (fakes). The multijet background normalisation and shape are estimated with a data-driven method, referred to as Matrix Method [95, 96]. This method uses the efficiencies of loosely selected leptons (loose leptons) to pass the default tight lepton selection cuts. The efficiencies are obtained in dedicated control regions enriched with real or non-prompt leptons, respectively, and applied to events selected with either loose or tight lepton definition to obtain the fraction of multijet events. Systematic uncertainties on the estimate are assessed using alternative control samples, propagating systematic uncertainties associated to object reconstruction and MC simulation to the fake-lepton estimate as well as by comparing different parametrisations of the efficiencies.

5 Analysis strategy

This search is focused on final states with a W-boson and a b-quark, coming from the decay of a singly-produced Q-quark. The signal events with single-lepton decay topology are characterised by the presence of one isolated lepton (electron or muon), at least one high-p_{T} b-jet with $p_{\mathrm{T}} > 350$ GeV and large missing

transverse momentum from the escaping neutrino. A requirement on the missing transverse momentum of $E_{\mathrm{T}}^{\mathrm{miss}} > 120$ GeV reduces the fraction of selected events originating from non-prompt or misidentified leptons as well as diboson events. To further exploit the low multiplicity of hard jets in the signal process, a cut on the number of jets in addition to the b-tagged jet is applied: events with any jet with $p_{\mathrm{T}} > 75$ GeV and $|\eta| < 2.5$ and satisfying ΔR (jet, leading b-tagged jet)< 1.2 or ΔR (jet, leading b-tagged jet) > 2.7 are rejected. This requirement reduces in particular background from production of $t\bar{t}$ events that are characterised by a higher multiplicity of high-p_{T} central jets, in contrast to signal events.

A requirement on the azimuthal separation between the lepton and the leading b-tagged jet, $|\Delta\phi$ (lepton, leading b-tagged jet)$| > 2.5$, increases the signal-to-background ratio because, in signal signatures, leptons from the leptonic W-boson decays recoil against the b-quark jet in the event. Furthermore, similar to t-channel single-top production, the single production of VLQs gives rise to a forward jet ($2.5 < |\eta| < 4.5$). Only events with at least one forward jet with a $p_{\mathrm{T}} > 40$ GeV are considered.

For a Y signal with a mass between 700 GeV and 1600 GeV and a coupling strength of $\sqrt{(c_{\mathrm{L}}^{Wb})^2 + (c_{\mathrm{R}}^{Wb})^2} \approx 1/\sqrt{2}$, the signal-to-background ratio (S/B) and the signal-to-background significance ratio (S/$\sqrt{\mathrm{B}}$) in the SR vary between 0.09 to 0.7 and 0.5 to 3.8, respectively. The acceptance times efficiency for these Y signals in the SR ranges from 0.3% to 1.4%.

The normalisation of W+jets processes, as well as the $t\bar{t}$ and single-top processes is partially constrained by fitting the predicted yields to data in CRs enriched in W and $t\bar{t}$ events. Two CRs are defined for this purpose, providing also samples depleted of expected signal events. The selection for the W+jets CR is the same as for the SR, except that each event is required to have exactly zero b-tagged jets and cuts related to the leading b-tagged jet are replaced with equivalent ones on the highest momentum jet. In addition the leading jet has a slightly lower transverse momentum requirement of $p_{\mathrm{T}} > 250$ GeV to increase the number of SM background events in this region. The selection for the $t\bar{t}$ CR is the same as for the SR, except that the leading b-tagged jet p_{T} must be greater than 200 GeV and that at least one hard jet with $p_{\mathrm{T}} > 75$ GeV and $|\eta| < 2.5$ is present fulfilling either ΔR (jet, b-tagged jet)< 1.2 or ΔR (jet, b-tagged jet) > 2.7. Table 2 summarises the main selection criteria of the event topologies in the SR and the orthogonal CRs. The contamination of the $t\bar{t}$ CR by Y/T signals with masses of ≥ 700 GeV is at most 5% and in the W+jets CR at most 1.5% for signals with a coupling strength of $\sqrt{(c_{\mathrm{L}}^{Wb})^2 + (c_{\mathrm{R}}^{Wb})^2} \approx 1/\sqrt{2}$.

A mismodelling of the W-boson transverse momentum is observed at high p_{T}. To correct for this mismodelling, reweighting factors are obtained at preselection for W+jet events as a function of the W-boson p_{T} and applied to the W+jets background in all kinematic distributions. The correction factors are approximately between 0.9 and unity for W-boson p_{T} below 300 GeV, going to 0.7- 0.8 for higher p_{T} values.

In the SR and CRs the invariant mass of the reconstructed VLQ candidate m_{VLQ} is used to discriminate the signal from the background processes in the statistical analysis. It is calculated from the leading b-tagged jet and the decay products of the leptonically-decaying W-boson candidate. The W-boson candidate is reconstructed by summing the four-momenta of the charged lepton and the neutrino. To obtain the z-component of the neutrino momentum ($p_{z,\nu}$), the invariant mass of the lepton-neutrino system is set to the W-boson mass and the resulting quadratic equation is solved. If no real solution exists, the $\vec{E}_{\mathrm{T}}^{\mathrm{miss}}$ vector is varied by the minimum amount required to produce exactly one real solution. If two real solutions are found, the one with the smallest $|p_{z,\nu}|$ is used. The W-boson candidate and the leading b-tagged jet are then used to reconstruct the Q candidate. For the W+jets CR the leading jet instead of the leading

Table 2: Summary of selection requirements that are changed for the $t\bar{t}$ and W+jets CRs compared to the SR requirements. All other requirements are the same for all three regions.

Region	Selection cuts:		
	Leading jet p_{T}	Leading jet is b-tagged	ΔR (jet, b-tagged jet))< 1.2 or ΔR (jet, b-tagged jet) > 2.7
SR	> 350 GeV	yes	0
$t\bar{t}$ CR	> 200 GeV	yes	≥ 1
W+jets CR	> 250 GeV	no	-

b-tagged jet is used for the m_{VLQ} calculation.

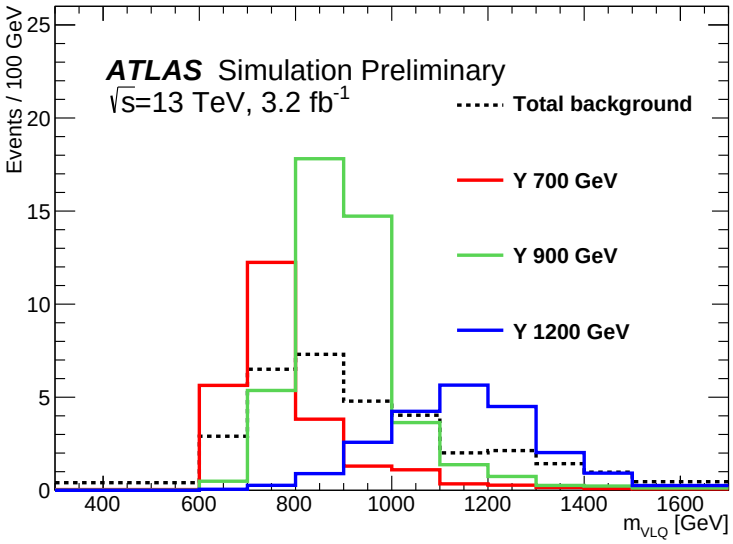

Figure 3: Distribution of VLQ candidate mass for three different signal masses in the SR for a coupling of $\sqrt{(c_{\mathrm{L}}^{Wb})^2 + (c_{\mathrm{R}}^{Wb})^2} \approx 1/\sqrt{2}$ together with the total SM background (black line).

Figure 3 shows the VLQ candidate invariant mass distribution in the SR for three simulated signal masses (700 GeV, 900 GeV, 1200 GeV) for a coupling of $\sqrt{(c_{\mathrm{L}}^{Wb})^2 + (c_{\mathrm{R}}^{Wb})^2} \approx 1/\sqrt{2}$, together with the total SM background. The distribution provides good discrimination between signal and background events in the SR. Given the large number of SM events in the CRs it also allows the combined effect of several systematic uncertainty sources to be constrained.

Figure 4(a) presents a data-to-SM comparison for the distribution of the VLQ candidate mass in the SR, while in Fig. 4(b) and 4(c) we provide the same distribution in the W+jets CR and in the $t\bar{t}$ CR, respectively. The distribution for a Y signal with a mass of 1200 GeV, scaled to the NLO theory cross-section assuming a coupling of $\sqrt{(c_{\mathrm{L}}^{Wb})^2 + (c_{\mathrm{R}}^{Wb})^2} \approx 1/\sqrt{2}$, is also shown. The binning of the presented

figures is the one optimised for the statistical procedure. The error band in all plots includes the statistical uncertainty on the Monte Carlo predictions and the total systematic uncertainties added in quadrature as discussed in Section 6. The figures show good agreement between the data and the SM background processes.

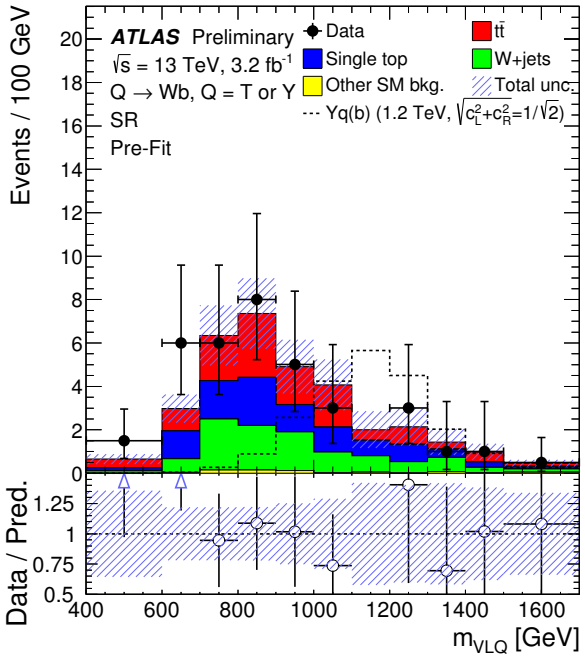

(a)

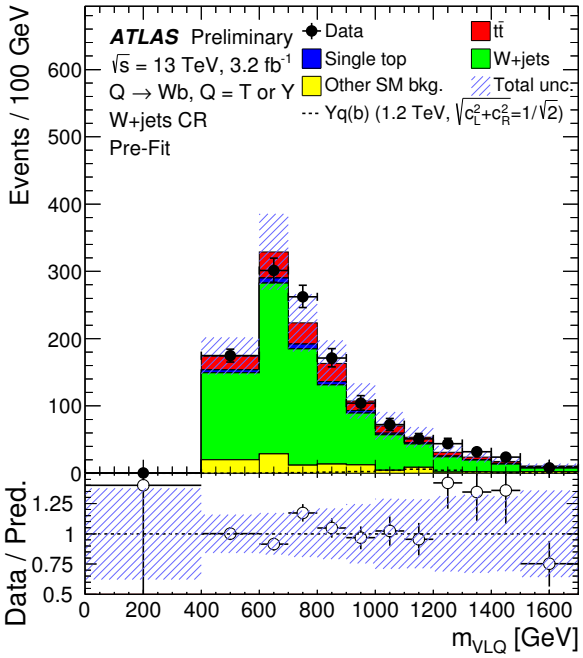

(b)

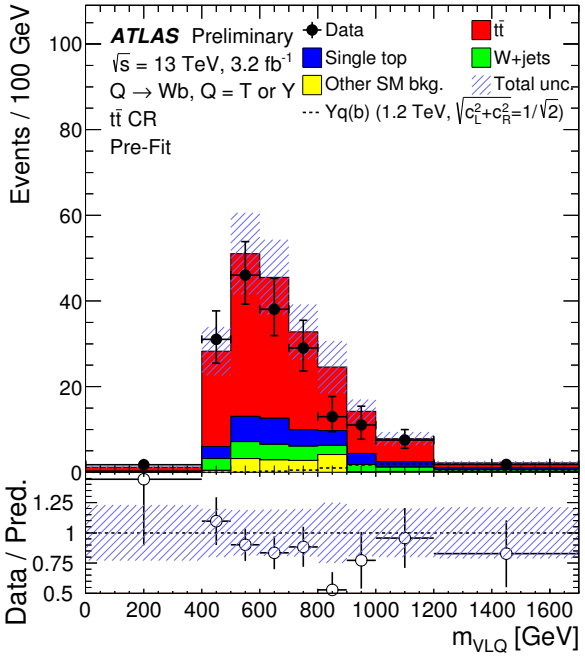

(c)

Figure 4: Distributions of the reconstructed VLQ mass m_{VLQ} in (a) the SR, (b) the W+jets CR, and (c) the $t\bar{t}$ CR for the SM background processes and data events. The signal distribution for a Y signal with a mass of 1200 GeV is scaled to the theory cross-section for a coupling of $\sqrt{(c_{\mathrm{L}}^{Wb})^2 + (c_{\mathrm{R}}^{Wb})^2} \approx 1/\sqrt{2}$. The uncertainty band includes the statistical uncertainty on the Monte Carlo predictions and the total systematic uncertainties added in quadrature. The first and last bin include the underflow and overflow, respectively.

6 Systematic uncertainties

Several sources of systematic uncertainty in this analysis can affect the normalisation of the signal and background and/or the shape of their corresponding m_{VLQ} distributions, which are used for the statistical study. They are included as nuisance parameters in the statistical analysis. Sources of uncertainty include the modelling of the detector response, object reconstruction algorithms, uncertainty on the theoretical modelling of the signals and backgrounds, as well as the uncertainty of the prediction arising from the limited size of the simulated event samples.

The following sections describe each of the systematic uncertainties considered in the search. Table 3 presents a summary of all systematic uncertainties considered in the analysis.

Systematic uncertainty	Type
Luminosity	N
Reconstructed objects	
Electron efficiency, energy scale, resolution	SN
Muon efficiency, momentum scale, resolution	SN
Jet vertex tagger	SN
Jet energy scale	SN
Jet energy resolution	SN
Missing transverse momentum	SN
b-tagging efficiency	SN
c-tagging efficiency	SN
Light-jet tagging efficiency	SN
Background model	
$t\bar{t}$ cross-section	N
$t\bar{t}$ modelling: ISR/FSR	SN
$t\bar{t}$ modelling: generator	SN
$t\bar{t}$ modelling: parton shower/hadronisation	SN
Single top cross-section	N
Single top modelling: ISR/FSR	SN
Single top modelling: generator	SN
Single top modelling: parton shower/hadronisation	SN
W+jets normalisation	N
W+jets modelling	SN
Z+jets normalisation	N
Diboson normalisation	N
Multijet normalisation	N

Table 3: List of systematic uncertainties considered in this analysis. An uncertainty taken as normalisation-only for all processes and channels affected is quoted as “N", whereas “SN" means that the uncertainty is taken to affect both shape and normalisation. Some of the systematic uncertainties are split into several components for a more accurate treatment.

6.1 Experimental uncertainties

The systematic uncertainty on the integrated luminosity for the 2015 dataset is ±2.1% and applied to all background and signal processes modelled using MC simulations. It is derived following the same methodology as that detailed in Refs. [33] from a calibration of the luminosity scale using a pair of $x - y$ beam-separation scans performed in August 2015.

Experimental sources of systematic uncertainty arise from the reconstruction and measurement of jets [45], leptons [36, 97] and $E_{\mathrm{T}}^{\mathrm{miss}}$ [98]. Uncertainties associated with leptons arise from the trigger, reconstruction, identification, and isolation efficiencies, as well as the lepton momentum scale and resolution, and are studied using $Z \to e^+e^-$ and $Z \to \mu^+\mu^-$ decays in data and simulation, while uncertainties associated with jets primarily arise from the jet energy scale (JES) and jet energy resolution. The JES and jet-energy resolution uncertainties [45] are derived by combining information from test-beam data, LHC collision data and simulation. Additional uncertainties are assessed in the extrapolation of the jet energy resolution from Run 1 to Run 2 conditions. The systematic uncertainty on the $E_{\mathrm{T}}^{\mathrm{miss}}$ reconstruction is dominated by the uncertainties on the energy calibration and resolution for reconstructed jets and leptons, which are propagated to $E_{\mathrm{T}}^{\mathrm{miss}}$ and thus are included in the systematic for the corresponding objects. In addition, uncertainty contributions on the scale and resolution of reconstructed tracks that are associated with the hard-scatter vertex but not associated to the hard term are considered.

The efficiency of the flavour tagging algorithm to correctly tag b-jets, or to mis-tag c-jets or light-flavor jets, is measured for each jet flavour using simulated control samples and in data $t\bar{t}$ events, D^* mesons, and jets with impact parameters and secondary vertices consistent with a negative lifetime, respectively. From these measurements, factors are defined to correct the tagging rates in the simulation [49, 50, 99]. The uncertainties associated with these measurements are factorized into statistically independent sources.

Although the flavour tagging systematic uncertainties are not large, the strong dependence on b-tagged jets in the analysis make these uncertainties the leading sources of experimental uncertainties (about 10.2% on the predicted background yield in the SR). Further large detector-specific uncertainties arise from JES uncertainties (about a 6% effect on the predicted background yield) and resolution uncertainties (3% on the predicted background yield). The total systematic uncertainty associated with $E_{\mathrm{T}}^{\mathrm{miss}}$ reconstruction is about 5% in the SR.

6.2 Theoretical modelling uncertainties

A number of systematic uncertainties affecting the modelling of $t\bar{t}$ and single top-quark processes are considered. Uncertainties associated with the modelling of the ISR and FSR are obtained by comparing the two alternative $t\bar{t}$ and single top-quark samples generated with Powheg-Box 2.0 + Pythia 6.428 with settings resulting in an increased and decreased amount of radiation compared to the nominal Powheg-Box 2.0 + Pythia 6.428 sample. An uncertainty associated with the choice of the NLO generator is derived by comparing two samples, one generated with Powheg-Box 2.0 + Herwig++ and another generated with Madgraph5_aMC@NLO and interfaced to Herwig++, and propagating the resulting fractional difference to the nominal Powheg-Box 2.0 + Pythia 6.428 prediction. Finally, an uncertainty due to the choice of parton shower and hadronisation model is derived for the $t\bar{t}$ background by comparing events produced by Powheg-Box 2.0 interfaced to Pythia 6.428 or Herwig++.

The normalisation of the $t\bar{t}$ and single-top backgrounds has an uncertainty of +5.7/-5.3% [79–84] and of 6.8% [88], respectively. Uncertainties affecting the modelling of the W/Z+jets background include a 5% effect from their respective normalisations to the theoretical NNLO cross-sections [100]. To account for the mismodelling of the W-boson p_{T} spectrum, reweighting factors are obtained at preselection for W+jet events. The m_{VLQ} distributions with and without applying these W-boson p_{T} correction factors for W+jet events are compared in the SR and CRs and the largest deviation in each bin is taken as a systematic uncertainty. An additional 25% normalisation uncertainty for W+jets events with $m_{\mathrm{VLQ}} > 1500$ GeV is applied in order to cover residual differences in the reweighted m_{VLQ} distribution in the preselected sample. In total the systematic uncertainty for the modelling of the Wp_{T} distribution is about 4%. The diboson background processes have an uncertainty of 5% from the NLO theoretical cross-sections [94, 101]. All normalisation uncertainties on the different background processes are treated as uncorrelated.

For background estimates based on simulations, the largest sources of theoretical modelling uncertainties are due to the choice of hard scattering generator (about 0.9–12% on the predicted background yield), varying the parameters controlling the initial and final state radiation (about 1–2% on the predicted background yield) and the choice of parton shower and hadronisation model (2–4%), where the theoretical modelling uncertainties from $t\bar{t}$ contribute the most.

The systematic uncertainties on the modelling of the high-mass Y/T signal sample that correspond to the choice of the PDF set are evaluated following the PDF4LHC15 prescription [85]. No further systematic uncertainties on the signal modelling and no uncertainties on the NLO signal production cross-section are considered. An additional uncertainty of 5% was applied to cover small differences in the reconstructed VLQ mass between signal samples passed through the full simulation of the ATLAS detector and for signal sample produced with a faster simulation (see Section 4).

6.3 Uncertainties for the multijet background

Uncertainties on the data-driven multijet background estimate include contributions from the uncertainty on the real and fake efficiencies extracted from data in dedicated CRs, uncertainties from the extrapolation from these CRs to the analysis regions and from the limited sample size in data [96]. While the multijet statistical uncertainty is considered together with the MC statistical uncertainty, the other two sources are assessed through a 50% normalisation uncertainty. No explicit shape uncertainty is assigned since the large statistical uncertainties associated with the multijet background prediction, which are uncorrelated bin-to-bin in the final discriminating variable, effectively cover shape uncertainties.

7 Results

7.1 Statistical interpretation

A binned maximum-likelihood fit to the data is performed in order to test for the presence of a signal. A separate fit is performed for each signal hypothesis with given mass and couplings. The inputs to the fit are the reconstructed VLQ candidate mass distribution m_{VLQ} in the SR and the two CRs. The binned likelihood function $\mathcal{L}(\mu, \theta)$ is constructed as a product of Poisson probability terms over all bins considered in the search. It depends on the signal-strength parameter μ, a multiplicative factor to the theoretical

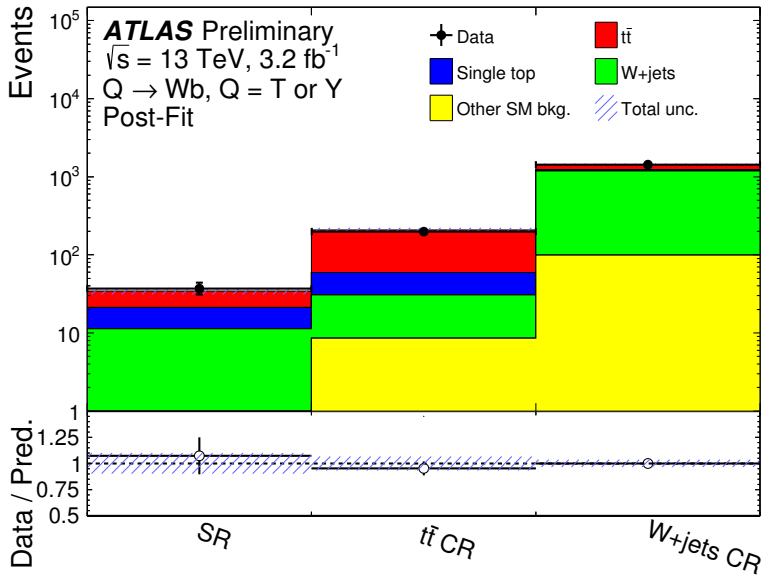

Figure 5: Observed and fitted background yields in the SR and in the two CRs. The lower panel shows the ratio between data and the fitted background yields. The error bars represent the statistical uncertainty on the data, the band represents the systematic uncertainty after the maximum likelihood fit.

signal production cross-section, and θ, a set of nuisance parameters that encode the effect of systematic uncertainties on the signal and background expectations and are implemented in the likelihood function as Gaussian constraints. Uncertainties in each bin of the m_{VLQ} distributions due to the finite statistics of the simulated samples are also considered by dedicated fit parameters and are propagated to μ. The nuisance parameters θ allow variations of the expectations for signal and background according to the corresponding systematic uncertainties, and their fitted values $\hat{\theta}$ correspond to the deviations from the nominal expectations that globally provide the best fit to the data. This procedure allows a reduction of the impact of systematic uncertainties on the search sensitivity by taking advantage of the highly populated background-dominated channels included in the likelihood fit. They also allow the CRs to improve the description of the data.

The test statistic q_μ is defined as the profile likelihood ratio: $q_\mu = -2\ln(\mathcal{L}(\mu, \hat{\hat{\theta}}_\mu)/\mathcal{L}(\hat{\mu}, \hat{\theta}))$, where $\hat{\mu}$ and $\hat{\theta}$ are the values of the parameters that maximise the likelihood function (with the constraint $0 \leq \hat{\mu} \leq \mu$), and $\hat{\hat{\theta}}_\mu$ are the values of the nuisance parameters that maximise the likelihood function for a given value of μ. In the absence of any significant excess above the background expectation, q_μ is used in the CL_s method [102, 103] to set an upper limit on the signal production cross-section times BR at the 95% CL. For a given signal scenario, values of the production cross-section (parametrised by μ) yielding $\mathrm{CL_s} < 0.05$, where $\mathrm{CL_s}$ is computed using the asymptotic approximation [104, 105], are excluded at 95% CL.

7.2 Fit results

The fit results for the yields in the SR and the two CRs are shown in Fig. 5. Figure 6 shows the m_{VLQ}

distribution after the background-only fit in the SR and the two CRs. Distributions of other kinematic variables after the fit in the SR, such as the transverse momentum of the leading b-tagged jet, the transverse momentum of the selected lepton, $E_{\mathrm{T}}^{\mathrm{miss}}$ and the transverse momentum of the reconstructed W-boson, are presented in Figure 7. Good agreement between the data and the SM backgrounds is found, in particular, in the SR for the m_{VLQ} distribution, where no peak above the predicted background is observed.

The total number of data events and the event yields after fitting the background-only hypotheses to data together with their systematic uncertainties in the signal region, are listed in Table 4.

	SR	$t\bar{t}$ CR	W+jets CR
$t\bar{t}$	13.4 ± 3.4	149.8 ± 14.8	195.5 ± 38.0
single top	9.8 ± 1.5	28.5 ± 4.0	42.0 ± 7.5
W+jets	10.7 ± 2.0	22.0 ± 4.4	1093.4 ± 59.1
Multijet	0.01 ± 0.3	5.4 ± 6.4	27.0 ± 16.3
Z+jets, diboson	0.6 ± 0.2	3.2 ± 0.6	72.2 ± 5.8
Total	34.5 ± 3.6	208.9 ± 15.6	1430.1 ± 52.1
Data	37	199	1427

Table 4: Event yields in the SR and the $t\bar{t}$ and W+jets CRs after the fit of the background-only hypothesis. The uncertainties include statistical and systematic uncertainties. The uncertainties on the individual background components can be larger than the uncertainty on the sum of the background, which is strongly constrained by the data.

7.3 Limits on the VLQ signal production

Since no significant excess over the expected SM background predictions is found, upper limits on the cross-section times branching ratio are set. Table 5 summarises the observed and expected (for the background-only hypothesis) 95% CL upper limits on the production cross-sections times branching ratio as a function of Q-quark mass, where the coupling $\sqrt{(c_{\mathrm{L}}^{Wb})^2 + (c_{\mathrm{R}}^{Wb})^2}$ was set to $\approx 1/\sqrt{2}$. The acceptance and fit result might change when the width of the VLQ Q is different from the one used in the MC simulation. It was explicitly checked using a truth level reweighting method (see section 4.1) that this effect is on the few percent level and would result in slightly more restrictive limits when taken into account.

Figure 8 shows the corresponding expected and observed upper limit at 95% CL on the cross-section times branching ratio for singly-produced VLQs decaying into Wb as a function of the mass of the VLQ Q. As a comparison, the theoretical prediction of the next-to-leading order (NLO) cross-section times branching ratio for VLQ production in bW fusion from Ref. [16] is shown, where the coupling $\sqrt{(c_{\mathrm{L}}^{Wb})^2 + (c_{\mathrm{R}}^{Wb})^2}$ was set to $\approx 1/\sqrt{2}$. For a coupling of $\sqrt{(c_{\mathrm{L}}^{Wb})^2 + (c_{\mathrm{R}}^{Wb})^2} \approx 1/\sqrt{2}$, the observed (expected) exclusion region for Q VLQ masses is smaller than 1.44 TeV (1.45 TeV).

The limit set on the cross-section times branching ratio can be translated into a limit on the NLO cross-section prediction for VLQ production in bW fusion [16], and the coupling using the relation

$$\sqrt{\frac{\sigma_{\mathrm{limit}}}{\sigma_{\mathrm{theory}}}} = \sqrt{(c_{\mathrm{L}}^{Wb})^2 + (c_{\mathrm{R}}^{Wb})^2} \tag{1}$$

Q Signal	Observed limit on $\sigma \times$ BR [pb]	-2σ	-1σ	Expected limit on $\sigma \times$ BR [pb]	+1σ	+2σ
700 GeV	1.70	0.58	0.35	1.26	0.57	1.38
800 GeV	0.79	0.33	0.20	0.70	0.39	1.02
900 GeV	0.33	0.17	0.10	0.37	0.17	0.41
1000 GeV	0.21	0.14	0.08	0.30	0.13	0.32
1100 GeV	0.16	0.12	0.07	0.26	0.12	0.29
1200 GeV	0.16	0.10	0.06	0.23	0.10	0.25
1300 GeV	0.22	0.11	0.07	0.24	0.11	0.27
1400 GeV	0.22	0.11	0.06	0.23	0.11	0.28
1500 GeV	0.26	0.11	0.07	0.24	0.12	0.31
1600 GeV	0.16	0.08	0.05	0.17	0.08	0.20

Table 5: Observed and expected (for the background-only hypothesis) 95% CL upper limits on the production cross-section times branching ratio ($\sigma \times$ BR) for various Q signals with masses of 500 GeV to 1600 GeV. The 68% and 95% confidence intervals around the expected limits under the background-only hypothesis are also provided, denoted by $\pm 1\sigma$ and $\pm 2\sigma$, respectively.

for a (B, Y) doublet and

$$\sqrt{\frac{(\sigma \times BR)_{\text{limit}}}{(\sigma \times BR)_{\text{theory}}}} = |c_L^{Wb}| \tag{2}$$

for a singlet T. The expected and observed limits on the couplings are shown in Fig. 9, for a T quark as a function of the T mass assuming BR($T \to Wb$) = 0.5, as well as for a Y quark as a function of the Y mass. The smallest coupling limits are set for masses around 1000 GeV, $\sqrt{(c_{\text{L}}^{Wb})^2 + (c_{\text{R}}^{Wb})^2} = 0.33$ for a Y quark and $|c_L^{Wb}| = 0.45$ for a T quark.

It is possible to translate the estimated limit on cross-sections times branching ratio to mixing parameter $\sin\theta_{R/L}$ limits. These limits on the mixing angle between the vector-like quark and the SM sector are derived in a similar fashion and are shown in Figure 10. In the case of the T singlet, the dependence of BR ($T \to Wb$) on $\sin\theta_L$ is explicitly taken into account in the translation from $\sigma \times$ BR to $\sin\theta_L$. As expected, it is found that BR ($T \to Wb$)$\approx$ 0.5 in the $\sin\theta_L$ and mass range under consideration. For a singlet T, exclusion limits on $|\sin\theta_L|$ range from 0.32 to 0.69 for masses of 1 to 1.5 TeV. For a (B, Y) doublet, exclusion limits on $|\sin\theta_R|$ vary between 0.23 and 0.56 for masses between 1 and 1.5 TeV. These direct bounds are also compared to those from electroweak precision observables taken from Ref. [6, 106] assuming no other multiplets besides the one considered. For the (B, Y) doublet model, the bounds presented here are close to these indirect constraints for masses between 900 and 1000 GeV.

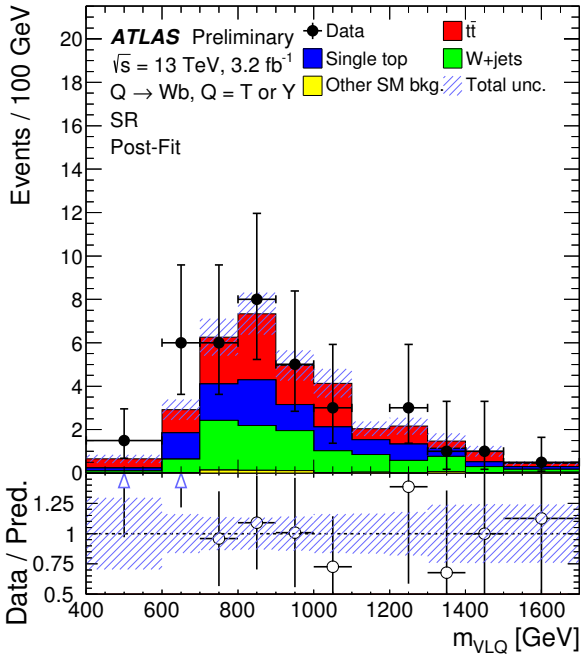

(a)

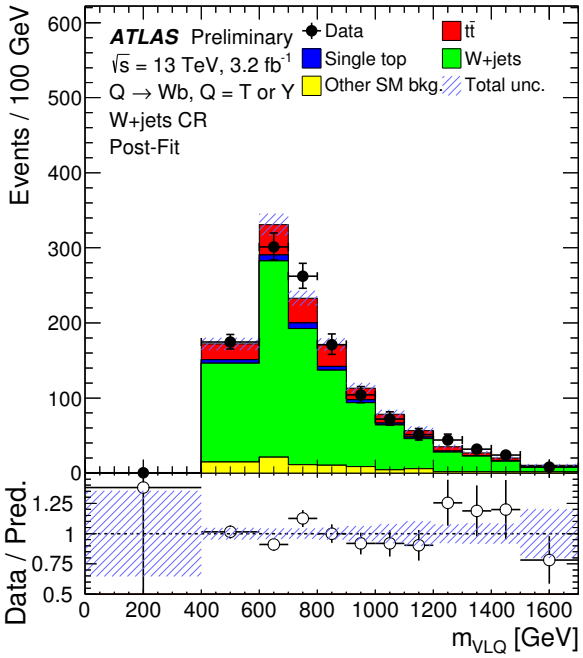

(b)

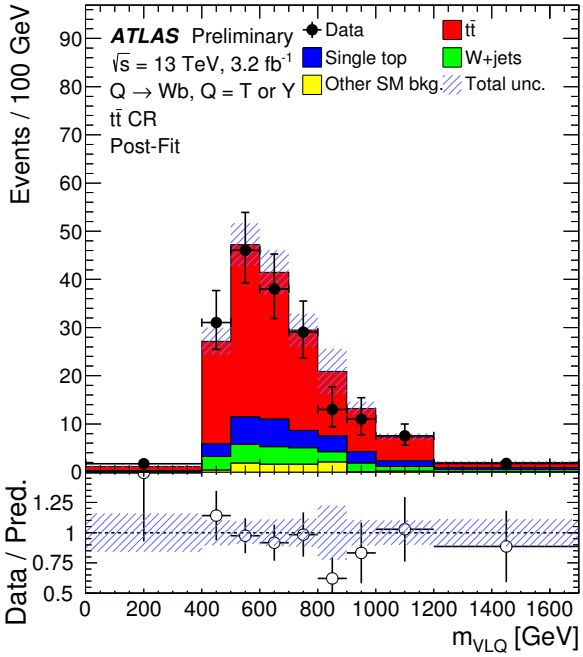

(c)

Figure 6: Fit result for the VLQ candidate mass distribution in (a) the SR, (b) the W+jets CR, and (c) the $t\bar{t}$ CR. The lower panels show the ratio between data and the fitted background yields. The error bars represent the statistical uncertainty on the data, the band represents the systematic uncertainty after the maximum likelihood fit.

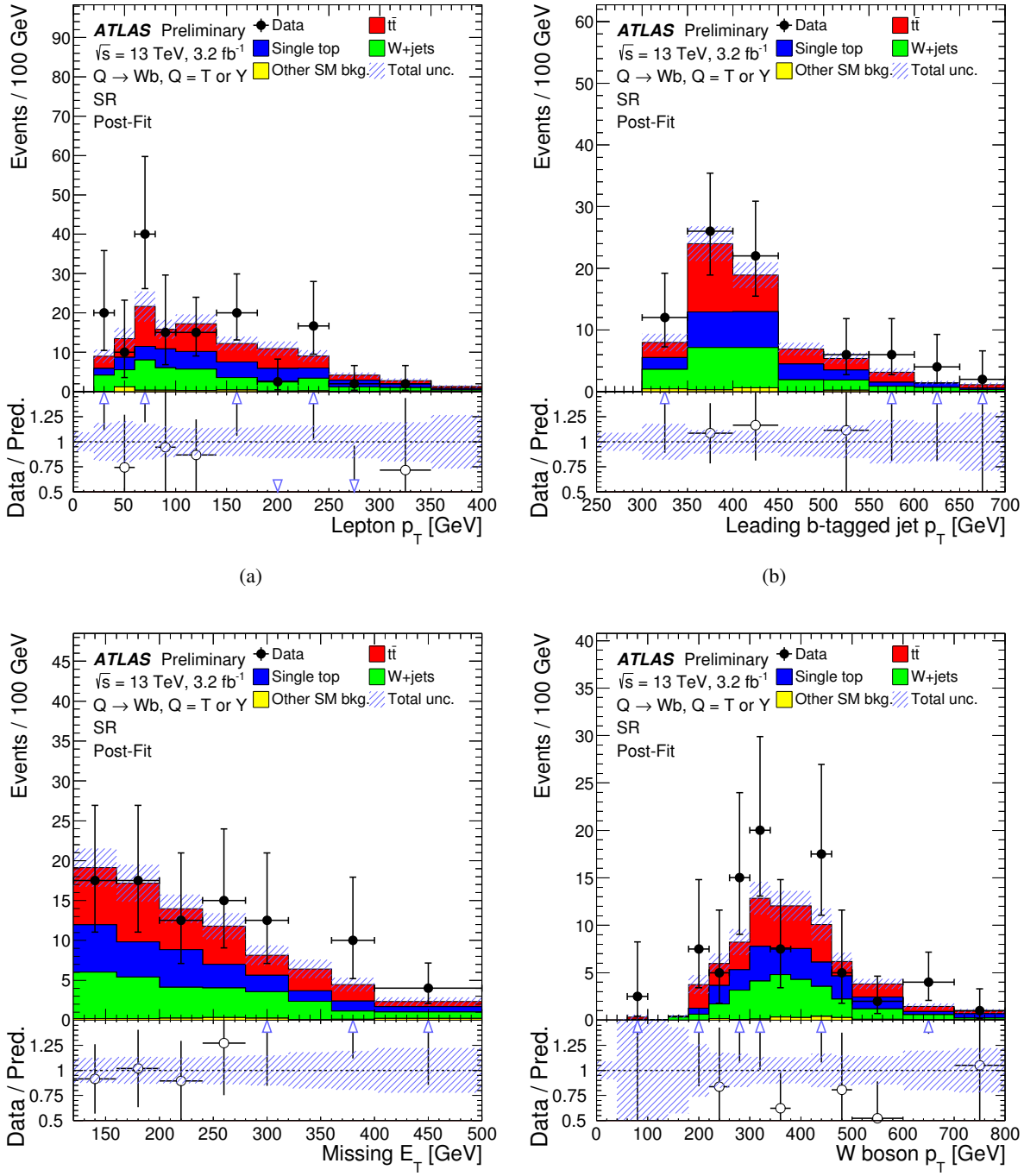

Figure 7: Distributions of (a) the lepton p_{T}, (b) the leading b-tagged jet, (c) the $E_{\mathrm{T}}^{\mathrm{miss}}$ and (d) the reconstructed W-boson p_{T} in the SR for data and the SM background processes with their post-fit normalisations. The uncertainty band includes statistical and all systematic uncertainties. The first and last bin include the underflow and overflow, respectively.

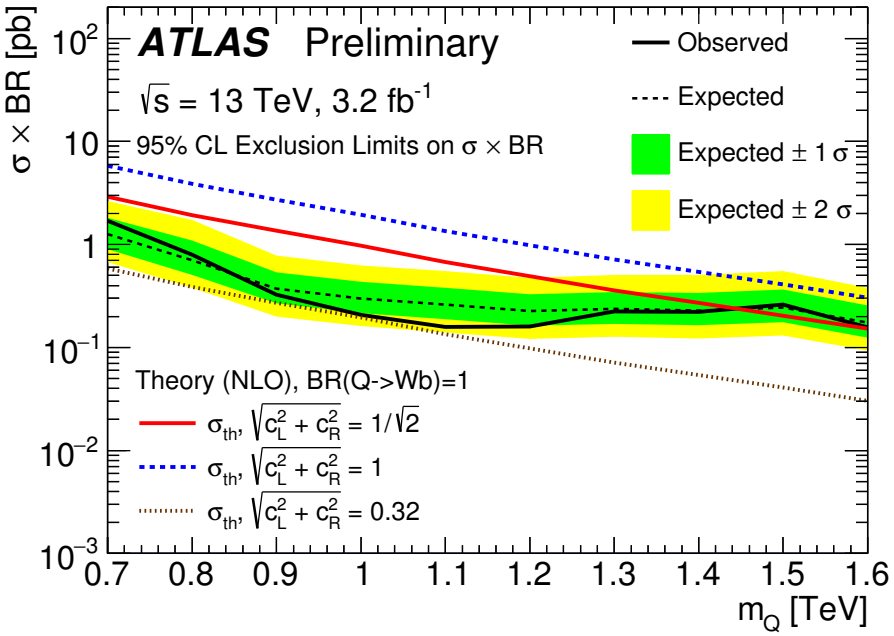

Figure 8: Expected (dashed black line) and observed (solid black line) upper limits at 95% CL on the cross-section times branching ratio as a function of the VLQ mass m_{Q}. The surrounding green and yellow bands correspond to ± 1 and ± 2 standard deviations around the expected limit. The solid red, blue dashed and brown dotted lines show the theoretical prediction of the NLO production cross-section from Ref. [16] for a coupling of $\sqrt{(c_{\mathrm{L}}^{Wb})^2 + (c_{\mathrm{R}}^{Wb})^2} = 1/\sqrt{2}$, $\sqrt{(c_{\mathrm{L}}^{Wb})^2 + (c_{\mathrm{R}}^{Wb})^2} = 1$ and $\sqrt{(c_{\mathrm{L}}^{Wb})^2 + (c_{\mathrm{R}}^{Wb})^2} = 0.32$, setting $\mathrm{BR}(Q \to Wb) = 1$.

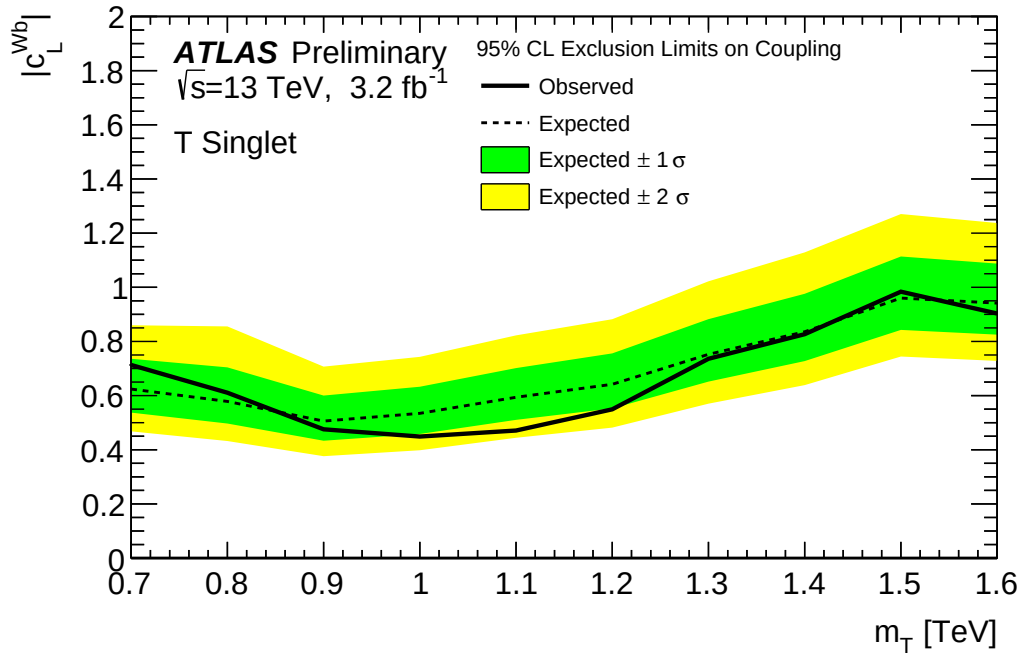

(a)

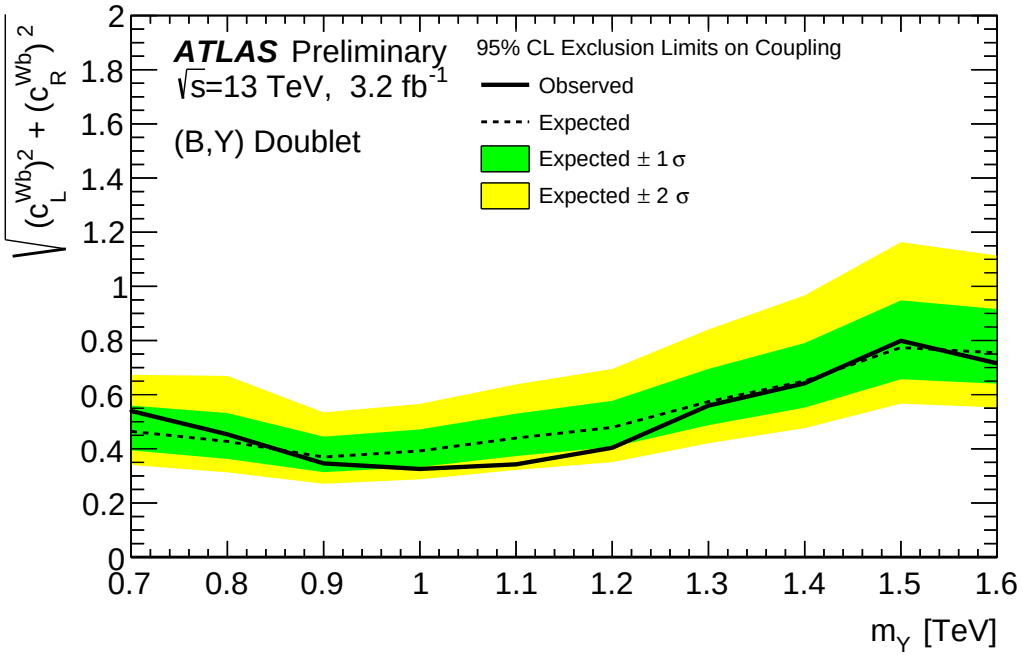

(b)

Figure 9: Expected (dashed black line) and observed (solid black line) 95% CL limits on the coupling of the vector-like quark to the SM W boson and a b-quark as a function of the VLQ mass m_Q between 700 GeV and 1600 GeV, where the BR $(Y/T \rightarrow Wb)$ is assumed to be (a) 50% for a singlet T-quark, and (b) 100% for a (B, Y) doublet model. The surrounding green and yellow bands correspond to ±1 and ±2 standard deviations around the expected limit. The excluded region is given by the area above the solid black line.

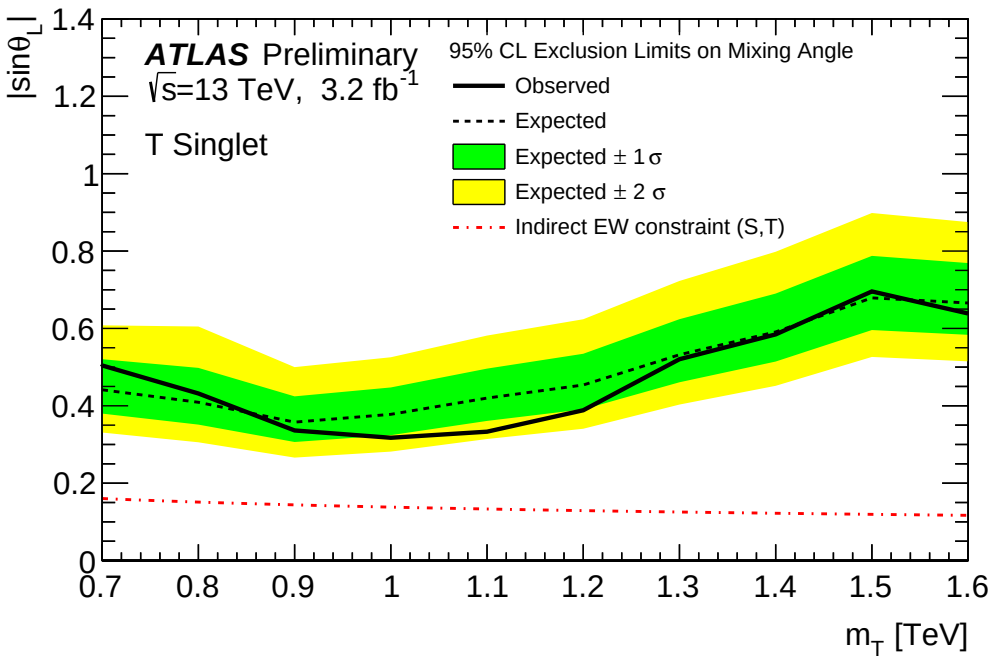

(a)

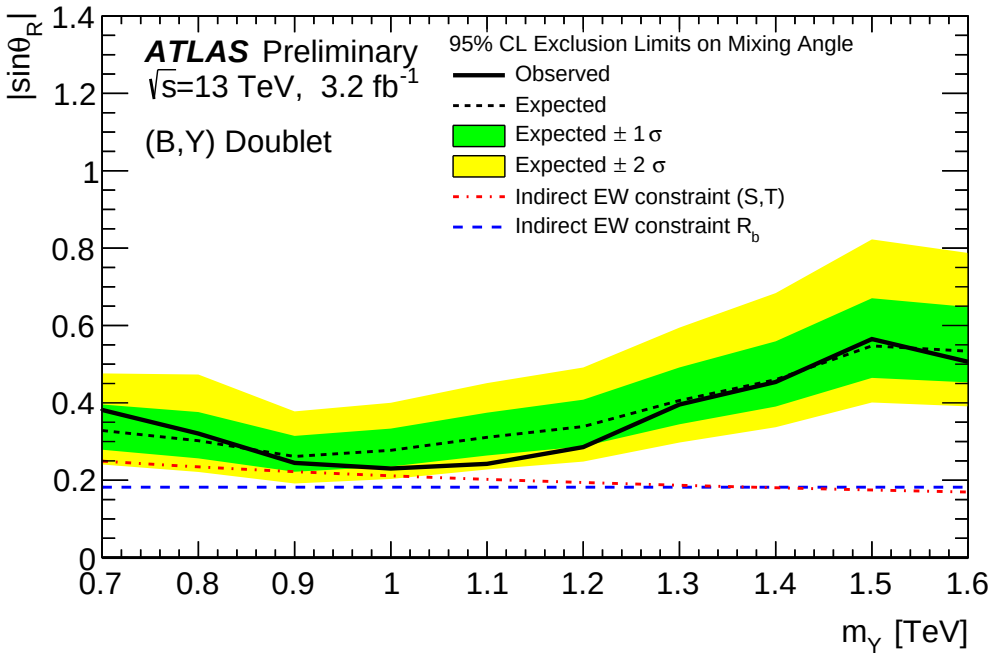

(b)

Figure 10: Expected (dashed black line) and observed (solid black line) 95% CL limits on (a) $|\sin\theta_L|$ for singlet T quark models assuming a BR ($T \to Wb$) ≈ 0.5 and (b) on $|\sin\theta_R|$ for (B,Y) doublet models assuming a BR ($Y \to Wb$) = 1.0 as a function of the VLQ mass m_Q between 700 GeV and 1600 GeV. The surrounding green and yellow bands correspond to ±1 and ±2 standard deviations around the expected limit. The excluded region is given by the area above the solid black line. As a comparison, constraints from electroweak precision observables taken from Ref. [6] are shown as well.

8 Conclusion

A search for the production of a single vector-like quark Q with subsequent decay into Wb has been carried out with the ATLAS experiment at the LHC. The data used in this search correspond to 3.2 fb^{-1}of pp collisions recorded in 2015 with the ATLAS detector at the CERN Large Hadron Collider at a centre-of-mass energy of $\sqrt{s}$ = 13 TeV. The selected events have exactly one isolated electron or muon, a high p_{T} b-tagged jet, large missing transverse momentum and at least one forward jet. The Q candidate is fully reconstructed and its mass is used as a discriminating variable in a maximum-likelihood fit. The observed data distributions are compatible with the Standard Model background prediction and no significant excess is observed. Upper limits at the 95% CL are set on the cross-section times branching ratio as a function of the VLQ mass. The results are also interpreted as limits on the QWb coupling strength and the mixing with the Standard Model sector for a singlet T-quark or a Y-quark from a (B, Y) doublet. For a QWb coupling strength of $\sqrt{(c_{\mathrm{L}}^{Wb})^2 + (c_{\mathrm{R}}^{Wb})^2} = 1/\sqrt{2}$, the observed (expected) 95% confidence level lower limit on the Y-quark mass is 1.44 TeV (1.45 TeV). Using theoretical predictions, the cross-section limits are translated into limits on the QWb couplings. The smallest coupling limits are set for a VLQ mass of 1000 GeV, $\sqrt{(c_{\mathrm{L}}^{Wb})^2 + (c_{\mathrm{R}}^{Wb})^2} = 0.33$ for a Y quark and $|c_L^{Wb}| = 0.45$ for a T quark. The results are also interpreted as a limit on the mixing parameter $|\sin\theta_{\mathrm{R}}|$ in a (B, Y) doublet model and $|\sin\theta_L|$ in a T singlet model. At a Y mass of 1000 GeV, the limit on $|\sin\theta_{\mathrm{R}}|$ is as low as 0.23 and close to the constraints from electroweak precision observables. For all signal scenarios explored, this analysis is found to significantly exceed the sensitivity of previous searches.

References

[1] B. Holdom et al., *Four Statements about the Fourth Generation*, PMC Phys. A 3 (2009) 4, arXiv: 0904.4698 [hep-ph].

[2] A. K. Alok, A. Dighe and D. London, *Constraints on the Four-Generation Quark Mixing Matrix from a Fit to Flavor-Physics Data*, Phys. Rev. D 83 (2011) 073008, arXiv: 1011.2634 [hep-ph].

[3] ATLAS Collaboration, *Observation of a new particle in the search for the Standard Model Higgs boson with the ATLAS detector at the LHC*, Phys. Lett. B 716 (2012) 1, arXiv: 1207.7214 [hep-ex].

[4] CMS Collaboration, *Observation of a new boson at a mass of 125 GeV with the CMS experiment at the LHC*, Phys. Lett. B 716 (2012) 30, arXiv: 1207.7235 [hep-ex].

[5] O. Eberhardt et al., *Impact of a Higgs boson at a mass of 126 GeV on the standard model with three and four fermion generations*, Phys. Rev. Lett. 109 (2012) 241802, arXiv: 1209.1101 [hep-ph].

[6] J. Aguilar-Saavedra et al., *Handbook of vectorlike quarks: Mixing and single production*, Phys. Rev. D 88 (2013) 094010, arXiv: 1306.0572 [hep-ph].

[7] F. del Aguila and M. J. Bowick, *The Possibility of New Fermions With $\Delta I = 0$ Mass*, Nucl. Phys. B 224 (1983) 107.

[8] G. Cacciapaglia et al., *Heavy Vector-like Top Partners at the LHC and flavour constraints*, JHEP 1203 (2012) 070, arXiv: 1108.6329 [hep-ph].

[9] M.-L. Xiao and J.-H. Yu, *Stabilizing Electroweak Vacuum in a Vector-like Fermion Model*, Phys. Rev. D 90 (2014) 014007, arXiv: 1404.0681 [hep-ph].

[10] L. Randall and R. Sundrum, *A Large mass hierarchy from a small extra dimension*, Phys. Rev. Lett. 83 (1999) 3370, arXiv: hep-ph/9905221 [hep-ph].

[11] D. B. Kaplan, H. Georgi and S. Dimopoulos, *Composite Higgs Scalars*, Phys. Lett. B 136 (1984) 187.

[12] N. Vignaroli, *Discovering the composite Higgs through the decay of a heavy fermion*, JHEP 1207 (2012) 158, arXiv: 1204.0468 [hep-ph].

[13] M. Schmaltz and D. Tucker-Smith, *Little Higgs review*, Ann. Rev. Nucl. Part. Sci. 55 (2005) 229, arXiv: hep-ph/0502182 [hep-ph].

[14] S. P. Martin, *Extra vector-like matter and the lightest Higgs scalar boson mass in low-energy supersymmetry*, Phys. Rev. D 81 (2010) 035004, arXiv: 0910.2732 [hep-ph].

[15] A. De Simone et al., *A First Top Partner Hunter's Guide*, JHEP 1304 (2013) 004, arXiv: 1211.5663 [hep-ph].

[16] O. Matsedonskyi, G. Panico and A. Wulzer, *On the Interpretation of Top Partners Searches*, JHEP 1412 (2014) 097, arXiv: 1409.0100 [hep-ph].

[17] M. E. Peskin and T. Takeuchi, *A New constraint on a strongly interacting Higgs sector*, Phys. Rev. Lett. 65 (1990) 964.

[18] ATLAS Collaboration, *Search for production of vector-like quark pairs and of four top quarks in the lepton-plus-jets final state in pp collisions at $\sqrt{s}$ = 8 TeV with the ATLAS detector*, JHEP 1508 (2015) 105, arXiv: 1505.04306 [hep-ex].

[19] ATLAS Collaboration, *Search for pair and single production of new heavy quarks that decay to a Z boson and a third-generation quark in pp collisions at $\sqrt{s}$ = 8 TeV with the ATLAS detector*, JHEP 1411 (2014) 104, arXiv: 1409.5500 [hep-ex].

[20] CMS Collaboration, *Search for vector-like T quarks decaying to top quarks and Higgs bosons in the all-hadronic channel using jet substructure*, JHEP 1506 (2015) 080, arXiv: 1503.01952 [hep-ex].

[21] CMS Collaboration, *Inclusive search for a vector-like T quark with charge 2/3 in pp collisions at $\sqrt{s}$ = 8 TeV*, Phys. Lett. B 729 (2014) 149, arXiv: 1311.7667 [hep-ex].

[22] CMS Collaboration, *Search for vector-like charge 2/3 T quarks in proton-proton collisions at $\sqrt{s}$ = 8 TeV*, Phys. Rev. D 93 (2016) 012003, arXiv: 1509.04177 [hep-ex].

[23] ATLAS Collaboration, *Analysis of events with b-jets and a pair of leptons of the same charge in pp collisions at $\sqrt{s}$ = 8 TeV with the ATLAS detector*, JHEP 1510 (2015) 150, arXiv: 1504.04605 [hep-ex].

[24] ATLAS Collaboration, *Search for single production of vector-like quarks decaying into Wb in pp collisions at $\sqrt{s}$ = 8 TeV with the ATLAS detector*, (2016, accepted by Eur. Phys. J. C), arXiv: 1602.05606 [hep-ex].

[25] ATLAS Collaboration, *Search for production of vector-like top quark pairs and of four top quarks in the lepton-plus-jets final state in pp collisions at $\sqrt{s}$ = 13 TeV with the ATLAS detector*, ATLAS-CONF-2016-013, 2016, URL: http://cds.cern.ch/record/2140998.

[26] CMS Collaboration, *Search for pair production of vector-like T quarks in the lepton plus jets final state*, CMS-PAS-B2G-16-002, 2016, URL: https://cds.cern.ch/record/2141070.

[27] CMS Collaboration, *Search for single production of vector-like quarks decaying into final states with a Z boson and a top or a bottom quark*, CMS-PAS-B2G-16-001, 2016, URL: https://cds.cern.ch/record/2199567.

[28] CMS Collaboration, *Search for a vectorlike top partner produced through electroweak interaction and decaying to a top quark and a Higgs boson using boosted topologies in the all-hadronic final state*, CMS-PAS-B2G-16-005, 2016, URL: https://cds.cern.ch/record/2160371.

[29] CMS Collaboration, *Search for Single Production of a Vector Like T Quark Decaying to a Higgs Boson and a Leptonically Decaying Top Quark*, CMS-PAS-B2G-15-008, 2016, URL: https://cds.cern.ch/record/2143233.

[30] ATLAS Collaboration, *The ATLAS Experiment at the CERN Large Hadron Collider*, JINST 3 (2008) S08003.

[31] M. Capeans et al., *ATLAS Insertable B-Layer Technical Design Report*, ATLAS-TDR-19, 2010, URL: https://cds.cern.ch/record/1291633.

[32] S. Artz et al., *Upgrade of the ATLAS Central Trigger for LHC Run-2*, JINST 10 (2015) C02030.

[33] ATLAS Collaboration, *Improved luminosity determination in pp collisions at $\sqrt{s}$ = 7 TeV using the ATLAS detector at the LHC*, Eur. Phys. J. C 73 (2013) 2518, arXiv: 1302.4393 [hep-ex].

[34] ATLAS Collaboration, *Electron reconstruction and identification efficiency measurements with the ATLAS detector using the 2011 LHC proton-proton collision data*, Eur. Phys. J. C 74 (2014) 2941, arXiv: 1404.2240 [hep-ex].

[35] ATLAS Collaboration, *Electron and photon energy calibration with the ATLAS detector using LHC Run 1 data*, Eur. Phys. J. C 74 (2014) 3071, arXiv: 1407.5063 [hep-ex].

[36] ATLAS Collaboration, *Electron identification measurements in ATLAS using $\sqrt{s}$ = 13 TeV data with 50 ns bunch spacing*, ATL-PHYS-PUB-2015-041, 2015, URL: https://cds.cern.ch/record/2048202.

[37] ATLAS Collaboration, *Measurement of the muon reconstruction performance of the ATLAS detector using 2011 and 2012 LHC proton–proton collision data*, Eur. Phys. J. C 74 (2014) 3130, arXiv: 1407.3935 [hep-ex].

[38] ATLAS Collaboration, *Muon reconstruction performance of the ATLAS detector in proton–proton collision data at $\sqrt{s}$ =13 TeV*, Eur. Phys. J. C 76 (2016) 292, arXiv: 1603.05598 [hep-ex].

[39] K. Rehermann and B. Tweedie, *Efficient Identification of Boosted Semileptonic Top Quarks at the LHC*, JHEP 1103 (2011) 059, arXiv: 1007.2221 [hep-ph].

[40] W. Lampl et al., *Calorimeter Clustering Algorithms: Description and Performance*, ATL-LARG-PUB-2008-002, 2008, URL: https://cds.cern.ch/record/1099735.

[41] M. Cacciari, G. Salam and G. Soyez, *The anti-k_t jet clustering algorithm*, JHEP 0804 (2008) 063, arXiv: 0802.1189 [hep-ph].

[42] C. Issever, K. Borras and D. Wegener, *An Improved weighting algorithm to achieve software compensation in a fine grained LAr calorimeter*, Nucl. Instrum. Meth. A 545 (2005) 803, arXiv: physics/0408129 [physics].

[43] ATLAS Collaboration, *Jet energy measurement with the ATLAS detector in proton-proton collisions at $\sqrt{s}$ = 7 TeV*, Eur. Phys. J. C 73 (2013) 2304, arXiv: 1112.6426 [hep-ex].

[44] ATLAS Collaboration, *Monte Carlo Calibration and Combination of In-situ Measurements of Jet Energy Scale, Jet Energy Resolution and Jet Mass in ATLAS*, ATLAS-CONF-2015-037, 2015, URL: https://cds.cern.ch/record/2044941.

[45] ATLAS Collaboration, *Jet Calibration and Systematic Uncertainties for Jets Reconstructed in the ATLAS Detector at $\sqrt{s}$ = 13 TeV*, ATL-PHYS-PUB-2015-015, 2015, URL: https://cds.cern.ch/record/2037613.

[46] ATLAS Collaboration, *Selection of jets produced in 13 TeV proton-proton collisions with the ATLAS detector*, ATLAS-CONF-2015-029, 2015, URL: https://cds.cern.ch/record/2037702.

[47] ATLAS Collaboration, *Performance of pile-up mitigation techniques for jets in pp collisions at $\sqrt{s}$ = 8 TeV using the ATLAS detector*, (2015, submitted to Eur. Phys. J. C), arXiv: 1510.03823 [hep-ex].

[48] ATLAS Collaboration,
Commissioning of the ATLAS b-tagging algorithms using $t\bar{t}$ events in early Run-2 data,
ATLAS-PHYS-PUB-2015-039, 2015, URL: http://cdsweb.cern.ch/record/2047871.

[49] ATLAS Collaboration,
Calibration of the performance of b-tagging for c and light-flavour jets in the 2012 ATLAS data,
ATLAS-CONF-2014-046, 2014, URL: https://cdsweb.cern.ch/record/1741020.

[50] ATLAS Collaboration, *Performance of b-Jet Identification in the ATLAS Experiment*,
JINST 11 (2016) P04008, arXiv: 1512.01094 [hep-ex].

[51] ATLAS Collaboration, *Expected performance of the ATLAS b-tagging algorithms in Run-2*,
ATL-PHYS-PUB-2015-022, 2015, URL: https://cds.cern.ch/record/2037697.

[52] ATLAS Collaboration, *Performance of missing transverse momentum reconstruction with the ATLAS detector in the first proton–proton collisions at* $\sqrt{s} = 13$ *TeV*,
ATL-PHYS-PUB-2015-027, 2015, URL: http://cdsweb.cern.ch/record/2037904.

[53] ATLAS Collaboration, *Performance of missing transverse momentum reconstruction in proton-proton collisions at 7 TeV with ATLAS*, Eur. Phys. J. C 72 (2012) 1844,
arXiv: 1108.5602 [hep-ex].

[54] ATLAS Collaboration, *The ATLAS Simulation Infrastructure*, Eur. Phys. J. C 70 (2010) 823,
arXiv: 1005.4568 [physics.ins-det].

[55] GEANT4 Collaboration, S. Agostinelli et al., *GEANT4: A Simulation toolkit*,
Nucl. Instrum. Meth. A 506 (2003) 250.

[56] ATLAS Collaboration, *The simulation principle and performance of the ATLAS fast calorimeter simulation FastCaloSim*, ATL-PHYS-PUB-2010-013, 2010,
URL: https://cds.cern.ch/record/1300517.

[57] T. Sjöstrand, S. Mrenna and P. Z. Skands, *A Brief Introduction to PYTHIA 8.1*,
Comput. Phys. Commun. 178 (2008) 852, arXiv: 0710.3820 [hep-ph].

[58] D. J. Lange, *The EvtGen particle decay simulation package*,
Nucl. Instrum. Meth. A 462 (2001) 152.

[59] T. Gleisberg et al., *Event generation with SHERPA 1.1*, JHEP 0902 (2009) 007,
arXiv: 0811.4622 [hep-ph].

[60] J. Alwall et al., *MadGraph 5 : Going Beyond*, JHEP 1106 (2011) 128,
arXiv: 1106.0522 [hep-ph].

[61] M. Botje et al., *The PDF4LHC Working Group Interim Recommendations*, (2011),
arXiv: 1101.0538 [hep-ph].

[62] T. Sjöstrand et al., *An Introduction to PYTHIA 8.2*, Comput. Phys. Commun. 191 (2015) 159,
arXiv: 1410.3012 [hep-ph].

[63] M. Buchkremer et al., *Model Independent Framework for Searches of Top Partners*,
Nucl. Phys. B 876 (2013) 376, arXiv: 1305.4172 [hep-ph].

[64] O. Matsedonskyi, G. Panico and A. Wulzer, *On the Interpretation of Top Partners Searches*,
JHEP 1412 (2014) 097, arXiv: 1409.0100 [hep-ph].

[65] A. Wulzer, *Cross section calculation for single Y production with decay to Wb*,
private communication (2015).

[66] P. Nason, *A New method for combining NLO QCD with shower Monte Carlo algorithms*, JHEP 0411 (2004) 040, arXiv: hep-ph/0409146 [hep-ph].

[67] S. Frixione et al., *Single-Top Production in MC@NLO*, JHEP 0603 (2006) 092, arXiv: hep-ph/0512250 [hep-ph].

[68] S. Alioli et al., *A general framework for implementing NLO calculations in shower Monte Carlo programs: the POWHEG BOX*, JHEP 1006 (2010) 043, arXiv: 1002.2581 [hep-ph].

[69] S. Frixione, P. Nason and G. Ridolfi, *A Positive-weight next-to-leading-order Monte Carlo for heavy flavour hadroproduction*, JHEP 0709 (2007) 126, arXiv: 0707.3088 [hep-ph].

[70] H. L. Lai et al., *New parton distributions for collider physics*, Phys. Rev. D 82 (2010) 074024, arXiv: 1007.2241 [hep-ph].

[71] T. Sjöstrand, S. Mrenna and P. Z. Skands, *PYTHIA 6.4 Physics and Manual*, JHEP 0605 (2006) 026, arXiv: hep-ph/0603175 [hep-ph].

[72] J. Pumplin et al., *New generation of parton distributions with uncertainties from global QCD analysis*, JHEP 0207 (2002) 012, arXiv: hep-ph/0201195 [hep-ph].

[73] P. Z. Skands, *Tuning Monte Carlo Generators: The Perugia Tunes*, Phys. Rev. D 82 (2010) 074018, arXiv: 1005.3457 [hep-ph].

[74] ATLAS Collaboration, *Comparison of Monte Carlo generator predictions to ATLAS measurements of top pair production at 7 TeV*, ATL-PHYS-PUB-2015-002, 2015, URL: https://cds.cern.ch/record/1981319.

[75] ATLAS Collaboration, *Comparison of Monte Carlo generator predictions from Powheg and Sherpa to ATLAS measurements of top pair production at 7 TeV*, ATL-PHYS-PUB-2015-011, 2015, URL: https://cds.cern.ch/record/2020602.

[76] M. Bahr et al., *Herwig++ Physics and Manual*, Eur. Phys. J. C 58 (2008) 639, arXiv: 0803.0883 [hep-ph].

[77] M. H. Seymour and A. Siodmok, *Constraining MPI models using σ_{eff} and recent Tevatron and LHC Underlying Event data*, JHEP 1310 (2013) 113, arXiv: 1307.5015 [hep-ph].

[78] J. Alwall et al., *The automated computation of tree-level and next-to-leading order differential cross sections, and their matching to parton shower simulations*, JHEP 1407 (2014) 079, arXiv: 1405.0301 [hep-ph].

[79] M. Czakon and A. Mitov, *Top++: A Program for the Calculation of the Top-Pair Cross-Section at Hadron Colliders*, Comput. Phys. Commun. 185 (2014) 2930, arXiv: 1112.5675 [hep-ph].

[80] M. Cacciari et al., *Top-pair production at hadron colliders with next-to-next-to-leading logarithmic soft-gluon resummation*, Phys. Lett. B 710 (2012) 612, arXiv: 1111.5869 [hep-ph].

[81] P. Bärnreuther, M. Czakon and A. Mitov, *Percent Level Precision Physics at the Tevatron: First Genuine NNLO QCD Corrections to $q\bar{q} \to t\bar{t}$*, Phys. Rev. Lett. 109 (2012) 132001, arXiv: 1204.5201 [hep-ph].

[82] M. Czakon and A. Mitov, *NNLO corrections to top-pair production at hadron colliders: the all-fermionic scattering channels*, JHEP 1212 (2012) 054, arXiv: 1207.0236 [hep-ph].

[83] M. Czakon and A. Mitov, *NNLO corrections to top-pair production at hadron colliders: the quark-gluon reaction*, JHEP 1301 (2013) 080, arXiv: 1210.6832 [hep-ph].

[84] M. Czakon, P. Fiedler and A. Mitov, *The total top quark pair production cross-section at hadron colliders through $O(\alpha_S^4)$*, Phys. Rev. Lett. 110 (2013) 252004, arXiv: 1303.6254 [hep-ph].

[85] J. Butterworth et al., *PDF4LHC recommendations for LHC Run II*, J. Phys. G 43 (2016) 023001, arXiv: 1510.03865 [hep-ph].

[86] R. Frederix, E. Re and P. Torrielli, *Single-top t-channel hadroproduction in the four-flavour scheme with POWHEG and aMC@NLO*, JHEP 1209 (2012) 130, arXiv: 1207.5391 [hep-ph].

[87] N. Kidonakis, *Next-to-next-to-leading-order collinear and soft gluon corrections for t-channel single top quark production*, Phys. Rev. D 83 (2011) 091503, arXiv: 1103.2792 [hep-ph].

[88] N. Kidonakis, *Two-loop soft anomalous dimensions for single top quark associated production with a W^- or H^-*, Phys. Rev. D 82 (2010) 054018, arXiv: 1005.4451 [hep-ph].

[89] N. Kidonakis, *NNLL resummation for s-channel single top quark production*, Phys. Rev. D 81 (2010) 054028, arXiv: 1001.5034 [hep-ph].

[90] T. Gleisberg and S. Höche, *Comix, a new matrix element generator*, JHEP 0812 (2008) 039, arXiv: 0808.3674 [hep-ph].

[91] F. Cascioli, P. Maierhofer and S. Pozzorini, *Scattering Amplitudes with Open Loops*, Phys. Rev. Lett. 108 (2012) 111601, arXiv: 1111.5206 [hep-ph].

[92] S. Schumann and F. Krauss, *A Parton shower algorithm based on Catani-Seymour dipole factorisation*, JHEP 0803 (2008) 038, arXiv: 0709.1027 [hep-ph].

[93] S. Höche et al., *QCD matrix elements + parton showers: The NLO case*, JHEP 1304 (2013) 027, arXiv: 1207.5030 [hep-ph].

[94] C. Anastasiou et al., *High precision QCD at hadron colliders: Electroweak gauge boson rapidity distributions at NNLO*, Phys. Rev. D 69 (2004) 094008, arXiv: hep-ph/0312266 [hep-ph].

[95] D0 Collaboration, B. Abbott et al., *Extraction of the width of the W boson from measurements of $\sigma(p\bar{p} \to W + X) \times B(W \to e\nu)$ and $\sigma(p\bar{p} \to Z + X) \times B(Z \to ee)$ and their ratio*, Phys. Rev. D 61 (2000) 072001, arXiv: hep-ex/9906025 [hep-ex].

[96] ATLAS Collaboration, *Estimation of non-prompt and fake lepton backgrounds in final states with top quarks produced in proton–proton collisions at $\sqrt{s} = 8$ TeV with the ATLAS Detector*, ATLAS-CONF-2014-058, 2014, URL: http://cdsweb.cern.ch/record/1951336.

[97] ATLAS Collaboration, *Muon reconstruction performance in early $\sqrt{s} = 13$ TeV data*, ATL-PHYS-PUB-2015-037, 2015, URL: http://cdsweb.cern.ch/record/2047831.

[98] B. H. Brunt et al., *Expected performance of missing transverse momentum reconstruction for the ATLAS detector at $\sqrt{s} = 13$ TeV*, ATL-PHYS-PUB-2015-023, 2015, URL: http://cds.cern.ch/record/2037700.

[99] ATLAS Collaboration, *Calibration of b-tagging using dileptonic top pair events in a combinatorial likelihood approach with the ATLAS experiment*, ATLAS-CONF-2014-004, 2014, URL: http://cdsweb.cern.ch/record/1664335.

[100] K. Melnikov and F. Petriello, *Electroweak gauge boson production at hadron colliders through $O(\alpha_S^2)$*, Phys. Rev. D 74 (2006) 114017, arXiv: hep-ph/0609070 [hep-ph].

[101] J. M. Campbell and R. K. Ellis, *An Update on vector boson pair production at hadron colliders*, Phys. Rev. D 60 (1999) 113006, arXiv: hep-ph/9905386 [hep-ph].

[102] T. Junk, *Confidence level computation for combining searches with small statistics*, Nucl. Instrum. Meth. A 434 (1999) 435, arXiv: hep-ex/9902006 [hep-ex].

[103] A. L. Read, *Presentation of search results: The CL_S technique*, J. Phys. G 28 (2002) 2693.

[104] G. Cowan et al., *Asymptotic formulae for likelihood-based tests of new physics*, Eur. Phys. J. C 71 (2011) 1554, arXiv: 1007.1727 [physics.data-an].

[105] G. Cowan et al., *Erratum to: Asymptotic formulae for likelihood-based tests of new physics*, Eur. Phys. J. C 73 (2013) 2501, arXiv: 1007.1727 [physics.data-an].

[106] J. Aguilar-Saavedra, *Constraints from electroweak precision observables*, private communication (2015).